

Theory and optical design of x-ray echo spectrometers

Yuri Shvyd'ko^{1,*}

¹*Advanced Photon Source, Argonne National Laboratory, Argonne, Illinois 60439, USA*

X-ray echo spectroscopy, a space-domain counterpart of neutron spin-echo, is a recently proposed inelastic x-ray scattering (IXS) technique. X-ray echo spectroscopy relies on imaging IXS spectra, and does not require x-ray monochromatization. Due to this, the echo-type IXS spectrometers are broad-band, and thus have a potential to simultaneously provide dramatically increased signal strength, reduced measurement times, and higher resolution compared to the traditional narrow-band scanning-type IXS spectrometers. The theory of x-ray echo spectrometers presented in [1] is developed here further with a focus on questions of practical importance, which could facilitate optical design and assessment of the feasibility and performance of the echo spectrometers. Among others, the following questions are addressed: spectral resolution, refocusing condition, echo spectrometers tolerances, refocusing condition adjustment, effective beam size on the sample, spectral window of imaging and scanning range, the impact of the secondary source size on the spectral resolution, the angular dispersive optics, the focusing and collimating optics, etc. Examples of optical designs and characteristics of echo spectrometers with 1-meV and 0.1-meV resolutions are presented.

PACS numbers: 07.85.Nc, 41.50.+h, 78.70.Ck, 07.85.Fv

I. INTRODUCTION

Photon and neutron inelastic scattering spectrometers are microscopes for imaging condensed matter dynamics at very small length and time scales. Momentum-resolved inelastic x-ray scattering (IXS) is a technique introduced [2, 3] and widely used [4–8] at storage-ring-based synchrotron radiation facilities. Despite numerous advances, progress on many of the key problems in condensed matter physics is held back because current inelastic scattering probes are limited in energy $\Delta\epsilon$, momentum ΔQ resolution, and in signal strength. The signal strength is limited by several factors. First, undulator spectral flux is at the limit of what is possible with current storage-ring-based x-ray source technology. High-repetition-rate self-seeded x-ray free-electron lasers in the future may provide orders of magnitude more spectral flux than what is possible at storage ring sources, and therefore may substantially improve IXS signal strength [9]. Second, because the signal strength $S \propto \Delta\epsilon^2 \Delta Q^2$ scales quadratically with the spectral and momentum transfer resolutions of traditional IXS instruments, it is severely limited by the small values of $\Delta\epsilon$ and ΔQ required for IXS. For example, improving the resolution by an order of magnitude from the currently available $\Delta\epsilon = 1.5$ meV and $\Delta Q = 1.5$ nm⁻¹ to a very much desired $\Delta\epsilon = 0.1$ meV and $\Delta Q = 0.1$ nm⁻¹ should inevitably result in a four orders of magnitude signal reduction. Such improvements in the resolutions of traditional IXS instruments seem, therefore, to be impractical at least at storage-ring-based x-ray sources.

A recently proposed x-ray echo spectroscopy technique can change the situation dramatically and open up completely new opportunities [1]. The essential features of

echo spectroscopy are, first, that it relies on imaging IXS spectra and, second, that it does not require x-ray monochromatization, as conventional IXS spectrometers do. Due to this, the echo-type IXS spectrometers may be broad-band devices, and therefore have a potential to simultaneously provide dramatically increased signal strength, reduced measurement times, and practical measurements having higher resolution.

In the present paper, we develop further the theory of the x-ray echo spectrometers with a focus on questions of practical importance, which could help in optical design and in assessing the feasibility and performance of echo spectrometers. Among others, the following questions are addressed: spectral resolution, refocusing condition, echo spectrometers tolerances, refocusing condition adjustment, effective beam size on the sample, spectral window of imaging and scanning range, the impact of secondary source size on the spectral resolution, the angular dispersive optics, the focusing and collimating optics etc.

Examples of optical designs and characteristics of x-ray echo spectrometers with 1-meV and 0.1-meV resolutions are presented and supported by the theory. In particular, the echo-type 0.1-meV-resolution IXS spectrometer is predicted to feature the same signal strength, however, a 10 times improved spectral resolution and a 25 times improved momentum transfer resolution (0.05 nm⁻¹) compared to a state-of-the-art narrow-band scanning-type 1-meV and 1-nm⁻¹ resolution IXS spectrometer [10, 11].

II. BASIC THEORY AND PRINCIPAL SCHEME

We start by considering optical systems featuring a combination of focusing and energy dispersing capabilities. We assume that such systems can, first, focus *monochromatic* x-rays from a source of a linear size Δx_0 in a source plane (reference plane 0 perpendicular to the optical axis z in Fig. 1) onto an intermediate image plane

*Electronic address: shvydko@aps.anl.gov

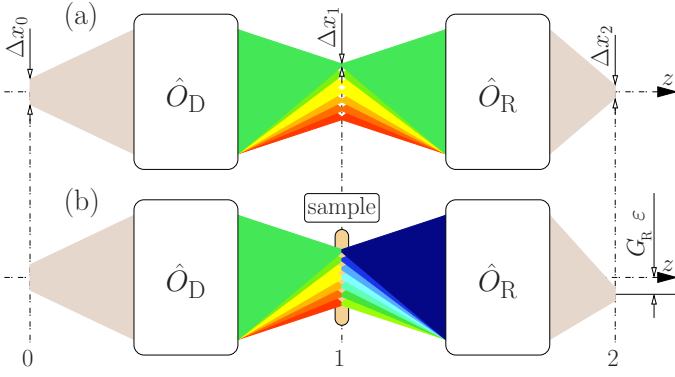


FIG. 1: Graphical presentation of the echo spectroscopy principles. (a) Photons from a source with a linear size Δx_0 in reference source plane 0 are focused onto a spot Δx_1 in the intermediate image plane 1 by a focusing-dispersing system \hat{O}_D . Each spectral component, indicated by different color, is focused at a different location due to dispersion in \hat{O}_D . All spectral components of the x-rays are refocused by a consecutive time-reversal focusing-dispersing system \hat{O}_R onto the same spot Δx_2 (echo) in the image plane 2. (b) Inelastic x-ray scattering with an energy transfer ε (indicated by changed color) from a sample in reference plane 1 results in a lateral shift $G_R \varepsilon$ of the echo signal equal for all spectral components.

(reference plane 1 in Fig. 1) with an image linear size $\Delta x_1 = |A|\Delta x_0$, where A is a magnification factor of the optical system. In addition, the system can disperse photons in such a way that the location of the image for photons with an energy $E + \delta E$ is displaced in the image plane by $G\delta E$ from the location of the image for photons with energy E . Here, G is a linear dispersion rate of the system, which is a product of the angular dispersion rate, hereafter denoted as \mathcal{D} , and a characteristic distance to the image plane. As a result, although monochromatic x-rays are focused, the whole spectrum of x-rays is defocused, due to linear dispersion.

We will use the ray-transfer matrix technique [12–14] to propagate paraxial x-rays through such optical systems and to determine linear and angular sizes of the x-ray beams along the optical axis. A paraxial ray in any reference plane is characterized by its distance x from the optical axis, by its angle ξ with respect to that axis, and the deviation δE of the photon energy from a nominal value E . The ray vector $\mathbf{r}_0 = (x_0, \xi_0, \delta E)$ at an input source plane is transformed to $\mathbf{r}_1 = (x_1, \xi_1, \delta E) = \hat{O}\mathbf{r}_0$ at the output reference plane (image plane), where $\hat{O} = \{ABG; CDF; 001\}$ is a ray-transfer matrix of an optical element placed between the planes. Only elastic processes in the optical systems are taken into account; that is reflected by zero and unity terms in the lowest row of the ray-transfer matrices.

Focusing of the monochromatic spectral components requires that matrix element $B = 0$. The ray-transfer matrix of any focusing-dispersing system in a general case

therefore reads as

$$\hat{O} = \{A \ 0 \ G; \ C \ D \ F; \ 001\} \quad (1)$$

with A and G elements defined above. The system blurs the polychromatic source image, because of linear dispersion, as mentioned earlier and graphically presented in Fig. 1(a). However, another focusing-dispersing system can be used to refocus the source onto reference plane 2. Indeed, propagation of x-rays through the defocusing system \hat{O}_D and a second system, which we will refer to as a refocusing or time-reversal system \hat{O}_R (see Fig. 1), is given by a combined ray-transfer matrix

$$\begin{aligned} \hat{O}_C &= \hat{O}_R \hat{O}_D = \{A_C \ 0 \ G_C; \ C_C D_C F_C; \ 001\} \\ &= \begin{pmatrix} A_R A_D & 0 & A_R G_D + G_R \\ C_R A_D + D_R C_D & D_R D_D & C_R G_D + D_R F_D + F_R \\ 0 & 0 & 1 \end{pmatrix}, \end{aligned} \quad (2)$$

and by a ray vector $\mathbf{r}_2 = (x_2, \xi_2, \delta E) = \hat{O}_C \mathbf{r}_0$.

Here we arrive at a crucial point. If

$$G_C = A_R G_D + G_R = 0, \quad (3)$$

the linear dispersion at the exit of the combined system vanishes, because dispersion in the defocusing system is compensated (time reversed) by dispersion in the refocusing system. As a result, the combined system refocuses all photons independent of the photon energy to the same location, x_2 in image plane 2, to a spot with a linear size

$$\Delta x_2 = |A_R A_D| \Delta x_0 \equiv |A_R| \Delta x_1, \quad (4)$$

as shown schematically in Fig. 1(a). Such behavior is an analog of the echo phenomena [15, 16]. Here, however, it takes place in space, rather than in the time domain.

Now, what happens if a sample is placed into the intermediate image plane 1, [Fig. 1(b)], which can scatter photons inelastically? In an inelastic scattering process, a photon with an arbitrary energy $E + \delta E$, changes its value to $E + \delta E + \varepsilon$. Here ε is an energy transfer in the inelastic scattering process. The ray vector $\mathbf{r}_1 = (x_1, \xi_1, \delta E)$ before scattering transforms to $\mathbf{r}'_1 = (x_1, \xi'_1, \delta E + \varepsilon)$ after inelastic scattering. Propagation of \mathbf{r}'_1 through the time-reversal system results in a ray vector $\mathbf{r}'_2 = (x'_2, \xi'_2, \delta E + \varepsilon) = \hat{O}_R \mathbf{r}'_1$. Assuming that refocusing condition (3) holds, we come to a decisive point: all photons independent of the incident photon energy $E + \delta E$ are refocused to the same location

$$x'_2 = x_2 + G_R \varepsilon, \quad x_2 = A_R A_D x_0, \quad (5)$$

which is, however, shifted from x_2 by $G_R \varepsilon$, a value proportional to the energy transfer ε in the inelastic scattering process. The essential point is that the combined defocusing-refocusing system maps the inelastic scattering spectrum onto image plane 2. The image is independent of the spectral composition $E + \delta E$ of the photons in the incident beam.

The spectral resolution $\Delta\varepsilon$ of the echo spectrometer is calculated from the condition that the shift due to inelastic scattering $x'_2 - x_2 = G_R\varepsilon$ is at least as large as the linear size Δx_2 of the echo signal in Eq. (4):

$$\Delta\varepsilon = \frac{\Delta x_2}{|G_R|} \equiv \frac{|A_R|\Delta x_1}{|G_R|} \equiv \frac{|A_R A_D|\Delta x_o}{|G_R|}. \quad (6)$$

Here it is assumed that the spatial resolution of the detector is better than Δx_2 . These results constitute the underlying principle of x-ray echo spectroscopy.¹ Most important is that the x-ray echo spectroscopy technique involves imaging the inelastic scattering spectrum without requiring x-ray monochromatization.

Perfect refocusing takes place if the linear dispersion of the combined system $G_C = A_R G_D + G_R$ vanishes, as in Eq. (3). Refocusing can still take place with good accuracy if $|G_C|$ is sufficiently small

$$|G_C|\Delta E \ll \Delta x_2, \quad (7)$$

and, therefore, does not deteriorate the spectral resolution. Here ΔE is a spectral bandwidth of x-rays in each *particular* point in image plane 2. In the following, ΔE will be referred to as an effective bandwidth of the spectrometer. It should not be confused with the spectral bandwidth ΔE_D of the defocusing system or the spectral window of imaging ΔE_R of the refocusing system. As discussed in Section V, ΔE is typically smaller than ΔE_D or ΔE_R . Tolerances on the echo spectrometer parameters, on the sample shape, etc., can be calculated with Eq. (7), as discussed in more detail in Section VI.

The above approach is general and applicable to any frequency domain. A particular version was proposed and realized in the soft x-ray domain, with diffraction gratings as dispersing elements [18, 19]. Our focus is IXS in the hard x-ray domain.² Diffraction gratings are not practical in the hard x-ray regime. However, the angular dispersion effect of the diffraction grating can be achieved in the hard x-ray regime by Bragg diffraction from *asymmetrically cut* crystals, i.e., from crystals with the reflecting atomic planes not parallel to the entrance surface, as demonstrated in [24, 25]. The crystals in asymmetric Bragg diffraction are *the* hard x-ray analog

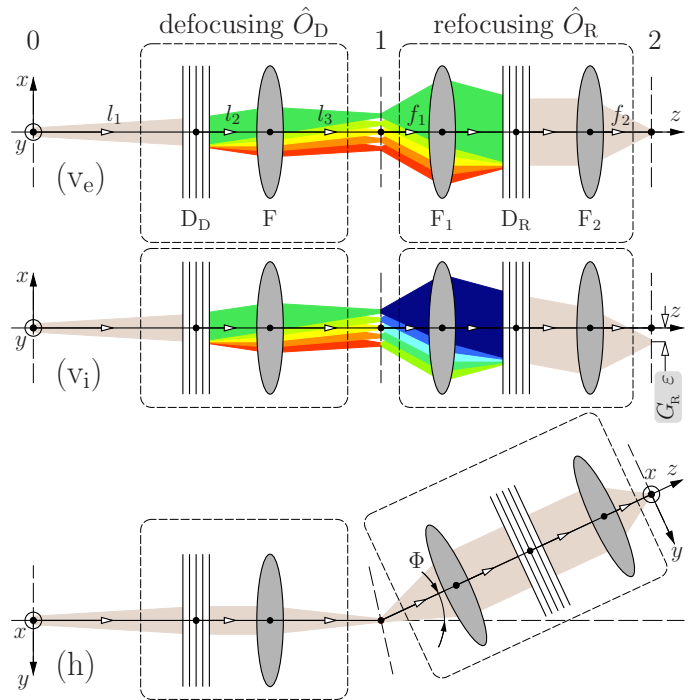


FIG. 2: Optical scheme of an x-ray echo spectrometer, comprised of the defocusing \hat{O}_D and refocusing \hat{O}_R dispersing systems; the x-ray source in reference plane 0; the sample in 1; and the position-sensitive detector in 2. The defocusing system \hat{O}_D consists of a dispersing Bragg diffracting (multi)crystal element D_D , and of a focusing element F . The refocusing system \hat{O}_R is of a spectrograph type comprising collimating element F_1 , a dispersing Bragg diffracting (multi)crystal element D_R , and an imaging element F_2 . The spectrometer is shown in the vertical dispersion plane (x, z) for elastic (v_e) and inelastic (v_i) scattering, and in the horizontal scattering plane (y, z) with the refocusing system at a scattering angle Φ (h). Φ defines the momentum transfer $Q = 2K \sin \Phi/2$ of a photon with momentum K .

of optical diffraction gratings or optical prisms. A large dispersion rate is a key for achieving high spectral resolution in angular-dispersive x-ray spectrometers [26, 27], including echo spectrometers; see Eq. (6). In the following two steps, we will show how the principal scheme of a generic echo spectrometer presented above, can be realized in the hard x-ray regime.

III. OPTICAL SCHEME

In the first step, we consider a more explicit optical scheme of the hard x-ray echo spectrometer, shown in Fig. 2, with the defocusing \hat{O}_D and refocusing \hat{O}_R dispersing systems equipped with specific optical elements. The x-ray source is in reference plane 0, the sample (secondary source) is in plane 1, and the position-sensitive detector is in plane 2. The defocusing system \hat{O}_D comprises a Bragg diffracting (multi)crystal dispersing ele-

¹ Noteworthy, angular dispersion always results in an inclined intensity front, i.e., in dispersion both perpendicular to and along the beam propagation direction [17]. Therefore, x-rays are defocused and refocused also in the time domain, as in spin-echo. As a result, inelastic scattering spectra can be also mapped by measuring time distributions in the detector, given a short-pulse source.

² Dispersion compensation was also applied to IXS spectrometers in the hard x-ray regime [20–23]. Because Bragg's law dispersion was compensated, the spectral resolution of the spectrometers was limited (to $\simeq 1$ -eV) by the Darwin widths of the Bragg reflections involved. The approach presented in this paper uses the angular dispersion, with the spectral resolution not limited by the Darwin width, and relies on broad-band IXS spectra imaging.

ment D_D and a focusing element F. As has been shown in [27], see also Table VI in Appendix A, such a system can be represented by a ray-transfer matrix (1) with the magnification A_D and linear dispersion G_D matrix elements given by

$$A_D = -\frac{1}{b_{U_D}} \frac{l_3}{l_{12}}, \quad G_D = \mathcal{D}_{U_D} \frac{l_3 l_1}{b_{U_D}^2 l_{12}}, \quad l_{12} = \frac{l_1}{b_{U_D}^2} + l_2. \quad (8)$$

Here, l_1 , l_2 , and l_3 are the distances between the x-ray source, the dispersing element D_D , the focusing element F with focal length $f = (l_{12}^{-1} + l_3^{-1})^{-1}$, and the sample in the image plane 1, respectively (Fig. 2). The dispersing (multi)crystal system D_D is characterized by the cumulative angular dispersion rate \mathcal{D}_{U_D} and cumulative asymmetry factor b_{U_D} , which are defined in [27] (see also Sec. IV A and Table VI in Appendix A).

For the spectrometer to feature a large throughput, the refocusing system \hat{O}_R has to be capable of collecting x-ray photons scattered from the sample in a large solid angle. An example of a focusing-dispersing system with a large solid acceptance angle is schematically shown in Fig 2. It is equivalent to the spectrograph scheme discussed in [27]. Collimating element F_1 with a focal distance f_1 collects photons in a large solid angle and makes x-ray beams of each spectral component parallel. The collimated beam impinges upon the Bragg (multi)crystal dispersing element D_R with the cumulative angular dispersion rate \mathcal{D}_{U_R} and the cumulative asymmetry factor b_{U_R} . Imaging element F_2 with a focal distance f_2 focuses x-rays onto the position-sensitive detector in image plane 2. As shown in [27] (see also Table VI in Appendix A), such a system is described by a ray-transfer matrix (1) with the magnification A_R and linear dispersion G_R matrix elements given by

$$A_R = -\frac{b_{U_R} f_2}{f_1}, \quad G_R = \mathcal{D}_{U_R} f_2. \quad (9)$$

Using Eqs. (3), (8), and (9), we obtain for the refocusing condition of the hard x-ray echo spectrometer schematically presented in Fig. 2:

$$\frac{l_3 l_1}{l_1 + b_{U_D}^2 l_2} \mathcal{D}_{U_D} = f_1 \frac{\mathcal{D}_{U_R}}{b_{U_R}}. \quad (10)$$

The dispersing element D_D can be placed from the source at a large distance $l_1 \gg b_{U_D}^2 l_2$. In this case, the refocusing condition (10) reads

$$l_3 \mathcal{D}_{U_D} \simeq f_1 \frac{\mathcal{D}_{U_R}}{b_{U_R}}. \quad (11)$$

We note that for the refocusing condition to be fulfilled, \mathcal{D}_{U_D} and $\mathcal{D}_{U_R}/b_{U_R}$ should have the same sign.

For the spectral resolution $\Delta\varepsilon$ of the hard x-ray echo spectrometer schematically presented in Fig. 2, we obtain from Eqs. (6), (8), and (9):

$$\Delta\varepsilon = \frac{|b_{U_R}|}{|\mathcal{D}_{U_R}|} \frac{\Delta x_1}{f_1}. \quad (12)$$

As follows from Eq. (12), the spectral resolution of the echo spectrometer is defined solely by the parameters of the refocusing system, and it is equivalent to the resolution of the hard x-ray spectrograph [27]. As pointed out before, the resolution is independent of the spectral composition of the x-rays impinging on the sample. The parameters of the defocusing system determine only the size of the secondary monochromatic source on the sample $\Delta x_1 = |A_D| \Delta x_0$, with A_D defined in Eq. (8).

Equation (12) can be used to estimate the magnitude of the dispersion rate of the dispersing element D_R or more precisely the ratio $|\mathcal{D}_{U_R}/b_{U_R}|$ required to achieve the desired spectral resolution. For example, for an x-ray echo spectrometer with a resolution $\Delta\varepsilon = 1$ meV, in the following referred to as XES1, the dispersing element D_R should feature $|\mathcal{D}_{U_R}/b_{U_R}| \simeq 25$ $\mu\text{rad}/\text{meV}$. For practical reasons, we assume here that the secondary *monochromatic* source size is $\Delta x_1 \simeq 5$ μm , which is presently routinely achievable, and the focal length of the collimating element in the refocusing system is $f_1 \simeq 0.2$ m, the value which ensures collection of x-rays scattered from the sample in a large solid angle. An x-ray echo spectrometer with a resolution $\Delta\varepsilon = 0.1$ meV, hereafter referred to as XES01, requires also a better momentum transfer resolution, i.e., a smaller solid angle of collection. Assuming, therefore, a larger focal distance $f_1 \simeq 0.4$ m, we obtain $|\mathcal{D}_{U_R}/b_{U_R}| \simeq 125$ $\mu\text{rad}/\text{meV}$ in this case. In the following, we will gradually specify parameters of the exemplary echo-type IXS spectrometers XES1 and XES01, and list them in Table V.

Now, with the $|\mathcal{D}_{U_R}/b_{U_R}|$ and f_1 values being specified, Eq. (11) can be used to estimate the required cumulative dispersing rate $|\mathcal{D}_{U_D}|$ of the dispersing element D_D . Assuming a comfortable distance $l_3 \simeq 2$ m from the focusing element F to the sample in the defocusing system, we estimate $|\mathcal{D}_{U_D}| \simeq 2.5$ $\mu\text{rad}/\text{meV}$ for spectrometer XES1 and $|\mathcal{D}_{U_D}| \simeq 25$ $\mu\text{rad}/\text{meV}$ for XES01, respectively.

IV. DISPERSIVE OPTIC

In the next step, we consider optical designs of the dispersing elements in the hard x-ray regime which could deliver the required values of the angular dispersion rates discussed in the previous section.

A. Angular dispersion rate

The angular dispersion rate $\mathcal{D} = d\theta'/dE$ measures the variation with photon energy E of the glancing angle of reflection θ' from the Bragg diffracting atomic planes, assuming the glancing angle of incidence θ (Bragg angle) is fixed. The angular dispersion rate [24, 28, 29]

$$\mathcal{D} = \frac{2 \sin \theta \sin \eta}{E \sin(\theta' - \eta)} \equiv -\frac{1}{E} (1 + b) \tan \theta. \quad (13)$$

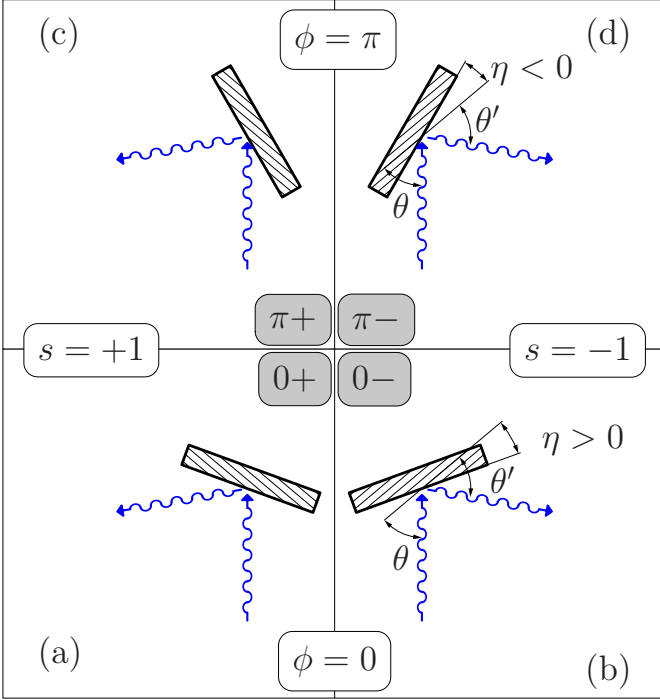


FIG. 3: Definition of scattering geometries in Bragg diffraction from asymmetrically cut crystals, with asymmetry angle η . Either geometry is specified by two parameters ϕ and s , each taking two possible values $\phi = 0, \pi$ and $s = \pm 1$: (a) $0+$, (b) $0-$, (c) $\pi+$, and (d) $\pi-$. The “deflection” sign $s = +1$ corresponds to reflection in the counterclockwise direction as in (a) and (c), while $s = -1$ means the clockwise direction as in (b) and (d). The azimuthal angle of incidence $\phi = 0$ (see definition in [24]) is equivalent here to a positive asymmetry angle η as in (a)-(b). The reversed scattering geometries shown in (c)-(d) correspond to $\phi = \pi$ and equivalently $\eta < 0$.

is nonzero only if the “asymmetry” angle η between the atomic planes and the crystal surface is nonzero. Here

$$b = -\frac{\sin(\theta + \eta)}{\sin(\theta' - \eta)} \quad (14)$$

is the asymmetry ratio. The angle η and its sign are defined in Fig. 3.

The dispersion rate is biggest, first, in Bragg backscattering when $\theta \rightarrow \pi/2$; second, when $\theta' - \eta \rightarrow 0$, i.e., when x-rays are reflected at grazing emergence to the crystal surface as in Figs. 3(a)-(b); and, third, for x-rays with smaller photon energies. In the following examples we use the (008) Bragg back reflection from Si of x-rays with photon energy $E \simeq 9.1$ keV. Such energy is optimal, ensuring sufficiently large dispersion rate and yet not too large photoabsorption in the optical elements and the sample.

The variation $d\theta'$ and the difference $|\theta - \theta'| \lesssim 10^{-5}$ are very small, and therefore in most cases θ' in Eqs. (13)-(14) can be replaced by θ .

The cumulative dispersion rate \mathcal{D}_{\cup_n} of a system of sequentially diffracting n crystals can be calculated using

the recursive relationship [27, 29]

$$\mathcal{D}_{\cup_n} = b_n \mathcal{D}_{\cup_{n-1}} + s_n \mathcal{D}_n, \quad (15)$$

with the deflection signs $s_n = \pm 1$ defined in Fig. 3. Remarkably, if the asymmetry ratio of the last n -th crystal is large $|b_n| \gg 1$, which can take place if $\eta > 0$ ($\phi = 0$) as in Figs. 3(a)-(b), the cumulative dispersion rate $\mathcal{D}_{\cup_{n-1}}$ of the previous $n - 1$ crystals can be amplified significantly, resulting in a very large cumulative dispersion rate \mathcal{D}_{\cup_n} of the whole system [29].

B. Single-crystal dispersing elements

The simplest x-ray dispersing element consists of one asymmetrically cut crystal. The largest attainable dispersion rate in Bragg diffraction of $\simeq 9$ keV x-rays from one crystal is $\mathcal{D} \lesssim 10 \mu\text{rad}/\text{meV}$. This follows from Eq. (13) by applying extreme but yet realistic values for $\theta \simeq 88^\circ\text{--}89^\circ$ and $\theta - \eta \gtrsim 1^\circ$. A one-crystal dispersing element is applicable if the required dispersion rate is smaller. This is the case of the dispersing element D_D of the defocusing system of the 1-meV-resolution spectrometer XES1 requiring $|\mathcal{D}_{\cup_D}| \simeq 2.5 \mu\text{rad}/\text{meV}$. Figure 4 shows an example of an optical design and spectral transmission function of the dispersing element. The function of the additional *symmetrically* cut ($\eta = 0$) crystal C is merely to keep the dispersed beam average direction after reflection from the asymmetrically cut crystal D parallel to the direction of the incident beam (in-line scheme).

C. Four-crystal CDDW dispersing elements

Dispersion elements with dispersion rates more than $\simeq 10 \mu\text{rad}/\text{meV}$ require multi-crystal solutions, ensuring dispersion rate enhancement according to Eq. (15). In [29] it was demonstrated that the angular dispersion rate of a four-crystal CDDW optic [26, 30, 31], schematically shown in Figs. 5, 6, and 7, can be dramatically enhanced by almost two orders of magnitude compared to what is possible with one asymmetrically cut crystal. The CDDW optic is not unique in achieving large dispersion rates. But, as discussed further in more detail, the CDDW optic is advantageous, as it features also a large angular acceptance, especially valuable for the refocusing dispersing element, and relatively large spectral bandwidths. The CDDW-type dispersing optics are therefore proposed here for use as large-dispersion-rate dispersing elements.

The in-line four-crystal CDDW-type dispersing optic comprises collimating (C), dispersing (D_1, D_2), and wavelength-selecting (W) crystals, which can be arranged in different scattering configurations. In the general case, a four-crystal scattering configuration can be defined as $(\phi_1 s_1, \phi_2 s_2, \phi_3 s_3, \phi_4 s_4)$. Here, for each crystal (C=1, $D_1 = 2$, $D_2 = 3$, W=4) the ϕ_n and s_n values

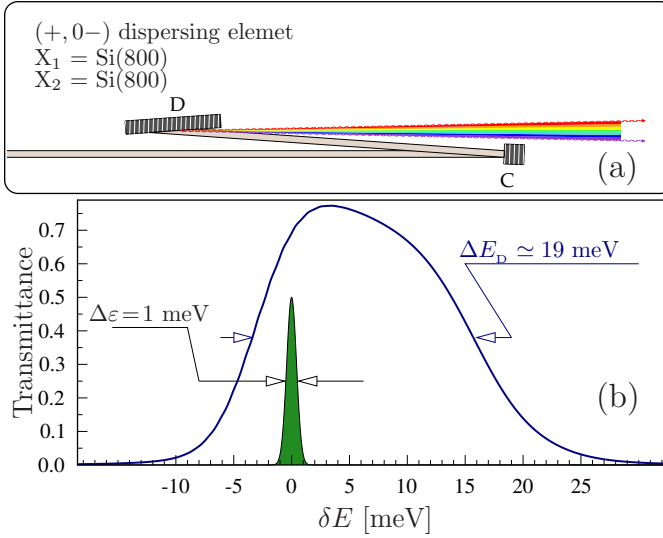


FIG. 4: X-ray dispersing element comprised of one asymmetrically cut crystal D (a) and its spectral transmittance function (b) calculated for the incident beam divergence of $20 \mu\text{rad}$. The symmetrically cut crystal C is added to ensure the in-line scheme. With the crystal parameters provided in Table I, the dispersing element features a spectral transmission function with a $\Delta E_D = 19$ meV bandwidth (b), a cumulative angular dispersion rate $\mathcal{D}_{UD} = -3.12 \mu\text{rad}/\text{meV}$, and a cumulative asymmetry factor $b_{UD} = 2.0$, appropriate for dispersing element D_D of the defocusing system \hat{O}_D (see Fig. 2) of the 1-meV-resolution x-ray echo spectrometer XES1. The sharp green line in (b) indicates the 1-meV design spectral resolution.

($n = 1, 2, 3, 4$) define the scattering geometry on each crystal, as in Fig. 3. Without loss of generality, we set for distinctness in all cases $s_1 = +1$. To ensure a large angular acceptance and collimation, which is possible if $|b_1| \ll 1$ is chosen for the first crystal, we set $\phi_1 = \pi$. To ensure large dispersion rate enhancement, a large $|b_4|$ is needed. Therefore, we set $\phi_4 = 0$. Of all the rest of the 32 possible cases ($\pi+, \phi_2 s_2, \phi_3 s_3, 0s_4$), those scattering geometries will be considered which feature an in-line scheme, the largest cumulative dispersion rate $|\mathcal{D}_{U_n}|$ for the dispersing element of the defocusing system, and the largest $|\mathcal{D}_{U_n}/b_{U_n}|$ value in case of the dispersing element of the refocusing system.

Following Eq. (15), the cumulative dispersion rate \mathcal{D}_{U_4} in a four-crystal system is given in the general case by

$$\mathcal{D}_{U_4} = b_4 b_3 b_2 s_1 \mathcal{D}_1 + b_4 b_3 s_2 \mathcal{D}_2 + b_4 s_3 \mathcal{D}_3 + s_4 \mathcal{D}_4. \quad (16)$$

Low-index Bragg reflections with small Bragg angles are typically chosen for the C- and W-crystals ($n = 1, 4$) to insure large angular acceptance and broadband transmission functions. On the contrary, high-index Bragg reflections with Bragg angles close to 90° are chosen to ensure the large dispersion rates of the D-crystals ($n = 2, 3$), which are typically much larger than those of the C- and W-crystals. Under these conditions, the expression for the cumulative dispersion rate can be reduced

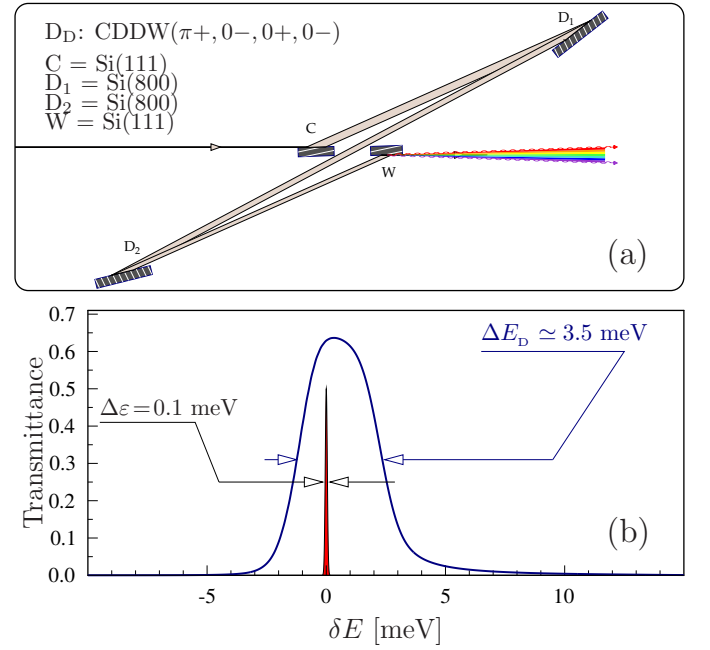


FIG. 5: In-line four-crystal CDDW-type x-ray dispersing element in a ($\pi+, 0-, 0+, 0-$) scattering configuration (a), and its spectral transmittance function (b) calculated for the incident beam divergence of $20 \mu\text{rad}$. With the crystal parameters provided in Table II, the optic features a spectral transmission function with a $\Delta E_D = 3.5$ meV bandwidth (b), a cumulative angular dispersion rate $\mathcal{D}_{UD} = -32 \mu\text{rad}/\text{meV}$, and a cumulative asymmetry factor $b_{UD} = 2$ appropriate for dispersing element D_D of the defocusing system \hat{O}_D (see Fig. 2) of the 0.1-meV-resolution x-ray echo spectrometer XES01. The sharp red line in (b) indicates the 0.1-meV design spectral resolution.

to $\mathcal{D}_{U_4} \simeq b_4 b_3 s_2 \mathcal{D}_2 + b_4 s_3 \mathcal{D}_3 = b_4 (b_3 s_2 \mathcal{D}_2 + s_3 \mathcal{D}_3)$. Since $b_3 < 0$, the largest dispersion rates can be achieved in the systems for which the product $s_2 s_3 \mathcal{D}_2 \mathcal{D}_3 < 0$. In this case, and assuming $|\mathcal{D}_2| = |\mathcal{D}_3|$, we obtain

$$\mathcal{D}_{U_4} \simeq b_4 s_3 \mathcal{D}_3 (1 - b_3). \quad (17)$$

Optical designs with $b_4 \simeq -20$, and $b_2 = b_3 \simeq -4$ may ensure enhancement of the cumulative dispersion rate of up to two orders of magnitude compared to what is possible with one crystal.

There are four large-dispersion-rate CDDW configurations featuring $\mathcal{D}_2 \mathcal{D}_3 < 0$ and $s_2 s_3 > 0$: ($\pi+, \pi-, 0-, 0-$); ($\pi+, \pi+, 0+, 0-$); ($\pi+, 0-, \pi-, 0-$); and ($\pi+, 0+, \pi+, 0-$). However, the angle between the incident and reflected beams is $4(\theta_2 - \pi/2)$, i.e. the beams impinging upon and emerging from the system are not parallel.

There are four other large-dispersion-rate CDDW configurations featuring $\mathcal{D}_2 \mathcal{D}_3 > 0$ and $s_2 s_3 < 0$: ($\pi+, \pi-, \pi+, 0-$); ($\pi+, \pi+, \pi-, 0-$); ($\pi+, 0-, 0+, 0-$); and ($\pi+, 0+, 0-, 0-$). These configurations are especially interesting, because the incident and transmitted x-rays are parallel (in-line scheme).

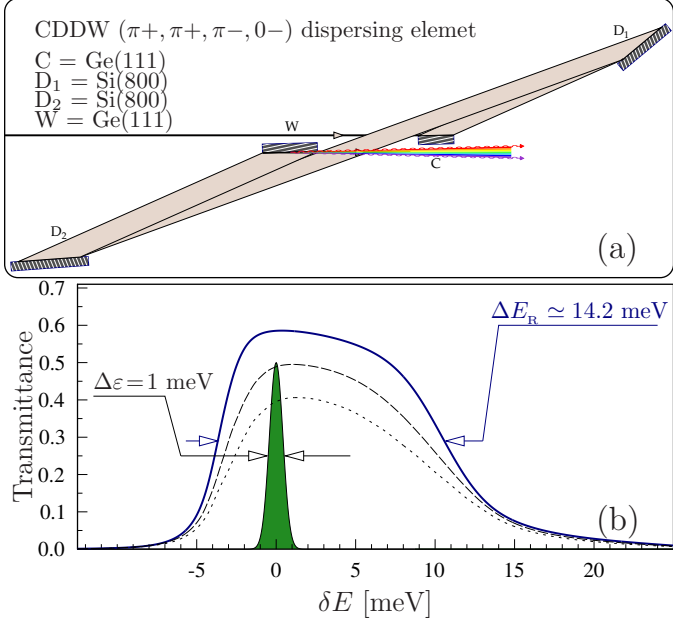


FIG. 6: In-line four-crystal CDDW-type x-ray dispersing element similar to that in Fig. 5 but in a $(\pi+, \pi+, \pi-, 0-)$ scattering configuration (a), and its spectral transmittance function (b) calculated for the incident beam divergence of 100 μrad (bold), 200 μrad (dashed), and 300 μrad (dotted). With the crystal parameters provided in Table I, the optic features a $\Delta E_R = 14.2$ meV bandwidth (b), a cumulative angular dispersion rate $\mathcal{D}_{U_R} = -16.47$ $\mu\text{rad}/\text{meV}$, a cumulative asymmetry factor $b_{U_R} = 0.65$, and $\mathcal{D}_{U_R}/b_{U_R} = -25.06$ $\mu\text{rad}/\text{meV}$, appropriate for dispersing element D_R of the refocusing system \hat{O}_R (see Fig. 2) of the 1-meV-resolution x-ray echo spectrometer XES1. The sharp line in (b) presents the 1-meV design spectral resolution $\Delta\epsilon$ of the x-ray echo spectrometer.

In the present paper, we choose the in-line large-dispersion-rate CDDW optic in the $(\pi+, 0-, 0+, 0-)$ configuration, with $|b_2| = |b_3| > 1$; see example in Fig. 5 for the dispersing elements D_D of the defocusing systems. This configuration is preferred as it provides large dispersion rates $|\mathcal{D}_{U_D}|$ [see Eq. (17)] significant transmission bandwidth ΔE_D , and compactness.

The CDDW optic in the $(\pi+, \pi+, \pi-, 0-)$ configuration, with $|b_2| = |b_3| < 1$ is better suited for the refocusing dispersing elements D_R (Figs. 6 and 7). It provides large absolute values of the ratio

$$\frac{\mathcal{D}_{U_4}}{b_{U_4}} \simeq -s_3 \mathcal{D}_3 \frac{1 - b_3}{b_1 b_2 b_3}. \quad (18)$$

required for the high spectral resolution of the echo spectrometers [see Eq. (12)], substantial transmission bandwidths $\Delta E_R/\Delta\epsilon \gg 1$, and large angular acceptance values $\Delta\theta_R \simeq 250$ μrad ; see Tables I and II.

Examples of the dispersing elements and their crystal parameters for the 1-meV-resolution x-ray echo spectrometer XES1 are provided in Figs. 4 and 6 and Table I. For the 0.1-meV-resolution x-ray echo spectrometer

| crystal element (e) | H_e | η_e | θ_e | $\Delta E_e^{(s)}$ | $\Delta\theta_e^{(s)}$ | b_e | $s_e \mathcal{D}_e$ |
|--|---------|----------|------------|--------------------|------------------------|-------------------|------------------------------------|
| [material] | (hkl) | deg | deg | meV | μrad | | $\frac{\mu\text{rad}}{\text{meV}}$ |
| D_D : $(+, 0-)$, Fig. 4 | | | | | | | |
| 1 C [Si] | (8 0 0) | 0 | 88 | 27 | 85 | -1.0 | 0 |
| 2 D [Si] | (8 0 0) | 84 | 88 | 27 | 85 | -2.0 | -3.12 |
| Cumulative values | | | | $\Delta\theta_D$ | ΔE_D | $\Delta\theta'_D$ | b_{U_D} |
| | | | | μrad | meV | μrad | $\frac{\mu\text{rad}}{\text{meV}}$ |
| | | | | 59 | 19 | 59.6 | 2.0 |
| | | | | | | | -3.12 |
| D_R : CDDW $(\pi+, \pi+, \pi-, 0-)$, Fig. 6 | | | | | | | |
| 1 C [Ge] | (1 1 1) | -10.5 | 12.0 | 3013 | 71 | -0.069 | -0.022 |
| 2 D_1 [Si] | (8 0 0) | -72.2 | 88 | 27 | 85 | -0.80 | -0.62 |
| 3 D_2 [Si] | (8 0 0) | -72.2 | 88 | 27 | 85 | -0.80 | +0.62 |
| 4 W [Ge] | (1 1 1) | 10.5 | 12.0 | 3013 | 71 | -14.8 | -0.31 |
| Cumulative values | | | | $\Delta\theta_R$ | ΔE_R | $\Delta\theta'_R$ | b_{U_R} |
| | | | | μrad | meV | μrad | $\frac{\mu\text{rad}}{\text{meV}}$ |
| | | | | 246 | 14.2 | 234 | 0.65 |
| | | | | | | | -16.5 |

TABLE I: Examples of in-line crystal optics as dispersing elements (“diffraction gratings”) D_D , D_R of the defocusing \hat{O}_D and refocusing \hat{O}_R systems of the 1-meV-resolution x-ray echo spectrometer XES1. For each optic, the table presents crystal elements (e=C, D_1 , D_2 , W) and their Bragg reflection parameters: (hkl), Miller indices of the Bragg diffraction vector H_e ; η_e , asymmetry angle; θ_e , glancing angle of incidence; $\Delta E_e^{(s)}$, $\Delta\theta_e^{(s)}$ Bragg reflection intrinsic spectral width and angular acceptance in symmetric scattering geometry, respectively; b_e , asymmetry ratio; and $s_e \mathcal{D}_e$, angular dispersion rate with deflection sign. For each optic, also shown are: angular acceptance $\Delta\theta_X$ (X=D, R) and spectral bandwidth ΔE_X as derived from the dynamical theory calculations, the angular spread of the dispersion fan $\Delta\theta'_X = |\mathcal{D}_{U_X}| \Delta E_X$, and the cumulative values of the asymmetry parameter b_{U_X} and the dispersion rate \mathcal{D}_{U_X} . X-ray photon energy is $E = 9.13708$ keV.

XES01, they are provided in Figs. 5 and 7 and Table II.

V. EFFECTIVE VERTICAL BEAM SIZE ON THE SAMPLE AND EFFECTIVE SPECTRAL BANDWIDTH

Each monochromatic spectral component is focused onto the sample in reference plane 1 to a spot with a vertical size of Δx_1 . However, different spectral components are focused at different positions distributed over a length of

$$\Delta X_D = |G_D| \Delta E_D \quad (19)$$

on the sample; see Fig. 8. Here ΔE_D is the total spectral width of x-rays incident on the sample. In the limit $\Delta x_1 \ll \Delta X_D$, which is considered here, the vertical beam size on the sample in the dispersion plane (x, z) is ΔX_D .

The effective vertical beam size ΔX_R as it is seen by the refocusing system may differ from ΔX_D . Particu-

| crystal element (e) | H_e | η_e | θ_e | $\Delta E_e^{(s)}$ | $\Delta\theta_e^{(s)}$ | b_e | $s_e \mathcal{D}_e$ |
|---|---------|----------|------------------|--------------------|------------------------|--------------|------------------------------------|
| [material] | (hkl) | deg | deg | meV | μrad | | $\frac{\mu\text{rad}}{\text{meV}}$ |
| D_D : CDDW ($\pi+, \pi+, \pi-, 0-$), Fig. 5 | | | | | | | |
| 1 C [Si] | (1 1 1) | -10.5 | 12.5 | 1304 | 32 | -0.09 | -0.02 |
| 2 D_1 [Si] | (8 0 0) | 77.7 | 88 | 27 | 85 | -1.38 | -1.19 |
| 3 D_2 [Si] | (8 0 0) | 77.7 | 88 | 27 | 85 | -1.38 | +1.19 |
| 4 W [Si] | (1 1 1) | 10.5 | 12.5 | 3013 | 71 | -11.2 | -0.24 |
| Cumulative values | | | $\Delta\theta_D$ | ΔE_D | $\Delta\theta'_D$ | $b_{\cup D}$ | $\mathcal{D}_{\cup D}$ |
| | | | μrad | meV | μrad | | $\frac{\mu\text{rad}}{\text{meV}}$ |
| | | | 57 | 3.5 | 112 | 1.91 | -31.7 |
| D_R : CDDW ($\pi+, \pi+, \pi-, 0-$), Fig. 7 | | | | | | | |
| 1 C [Ge] | (1 1 1) | -10.5 | 12.0 | 3013 | 71 | -0.07 | -0.02 |
| 2 D_1 [Si] | (8 0 0) | -83.75 | 88 | 27 | 85 | -0.52 | -1.50 |
| 3 D_2 [Si] | (8 0 0) | -83.75 | 88 | 27 | 85 | -0.52 | +1.50 |
| 4 W [Ge] | (1 1 1) | 10.5 | 12.0 | 3013 | 71 | -14.75 | -0.31 |
| Cumulative values | | | $\Delta\theta_R$ | ΔE_R | $\Delta\theta'_R$ | $b_{\cup R}$ | $\mathcal{D}_{\cup R}$ |
| | | | μrad | meV | μrad | | $\frac{\mu\text{rad}}{\text{meV}}$ |
| | | | 262 | 8 | 272 | 0.27 | -34.15 |

TABLE II: Same as Table I, but for the 0.1-meV-resolution x-ray echo spectrometer XES01.

larly, this happens if the spectral bandwidth ΔE_R of the refocusing system is smaller than ΔE_D . In this case, the effective beam size ΔX_R is smaller than ΔX_D [see Fig. 8(a)] and is given by

$$\Delta X_R = |G_D| \Delta E_R \equiv \left| \frac{\mathcal{D}_{\cup R}}{b_{\cup R}} \right| f_1 \Delta E_R. \quad (20)$$

The right-hand side of Eq. (20) is derived from the refocusing condition Eq. (3) and Eq. (9). Further, applying Eq. (12), the effective beam size ΔX_R can be presented in an equivalent form

$$\Delta X_R = \Delta x_1 \frac{\Delta E_R}{\Delta \varepsilon}, \quad (21)$$

expressed through the required spectral resolution $\Delta \varepsilon$ of the spectrometer and the secondary source size Δx_1 .

The effective beam size on the sample can become even smaller. Indeed, if the angular acceptance $\Delta \theta_R$ of the dispersing element D_R is smaller than the effective angular spread $\simeq \Delta X_R / f_1$ of the beam incident on D_R , then the effective beam size accepted by the refocusing system is further reduced to

$$\Delta X \simeq f_1 \Delta \theta_R; \quad (22)$$

see Fig. 8(b).

By the same reasoning, the spectral bandwidth of the incident beam seen by the refocusing system in each point of the detector plane is therefore reduced from ΔE_R to a

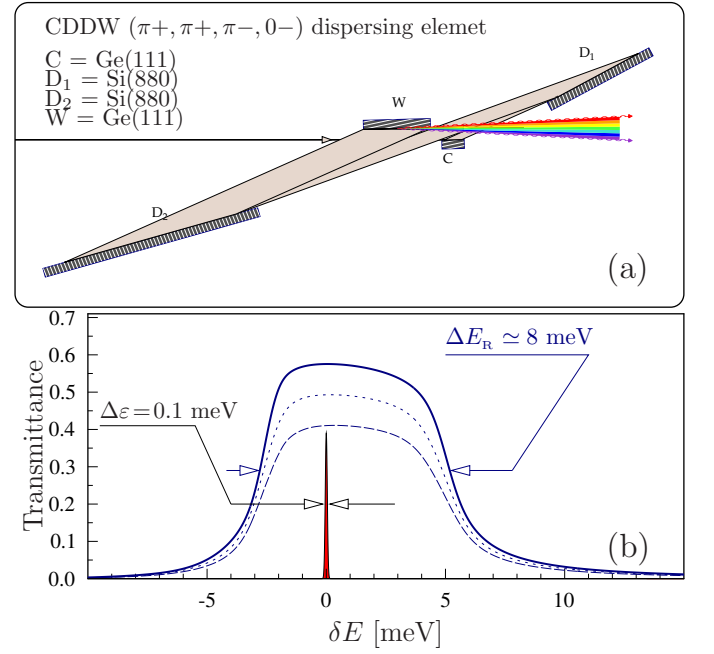


FIG. 7: In-line four-crystal CDDW-type x-ray dispersing element in a ($\pi+, \pi+, \pi-, 0-$) scattering configuration (a), and its spectral transmittance function (b) calculated for the incident beam divergence of 100 μrad (bold), 200 μrad (dashed), and 300 μrad (dotted). With the crystal parameters provided in Table II, the optic features a $\Delta E_R = 8$ meV bandwidth (b), a cumulative angular dispersion rate $\mathcal{D}_{\cup R} = -34.2 \mu\text{rad}/\text{meV}$, a cumulative asymmetry factor $b_{\cup R} = 0.27$, and $\mathcal{D}_{\cup R}/b_{\cup R} = -125.5 \mu\text{rad}/\text{meV}$, appropriate for dispersing element D_R of the refocusing system \hat{O}_R (see Fig. 2) of the 0.1-meV-resolution x-ray echo spectrometer XES01. The sharp line in (b) presents the 0.1-meV design spectral resolution $\Delta \varepsilon$ of the x-ray echo spectrometer.

smaller effective bandwidth $\Delta E = \Delta E_R \Delta X / \Delta X_R$. Using Eqs. (20)-(22), it can be presented as

$$\Delta E = \left| \frac{b_{\cup R}}{\mathcal{D}_{\cup R}} \right| \Delta \theta_R. \quad (23)$$

Of all the incident photons on the sample, the spectrometer can therefore use only those within the effective spectral bandwidth ΔE , rather than within ΔE_D . In this regard, it is also important to note that although the effective spectral bandwidth of the incident photons is reduced to ΔE because of a limited angular acceptance $\Delta \theta_R$ of the dispersing element D_R , the spectral window of imaging is still intact and equal to the spectral bandwidth ΔE_R of the refocusing system. The gain in signal strength of an echo spectrometer compared to a conventional narrow-band scanning spectrometer with the same spectral resolution $\Delta \varepsilon$ can be therefore estimated as

$$\mathcal{G} = \frac{\Delta E}{\Delta \varepsilon} \frac{\Delta E_R}{\Delta \varepsilon}. \quad (24)$$

Assuming the angular acceptance of D_R is $\Delta \theta_R \simeq 250 \mu\text{rad}$ (see Table V), we obtain $\Delta X \simeq 50 \mu\text{m}$, $\Delta E =$

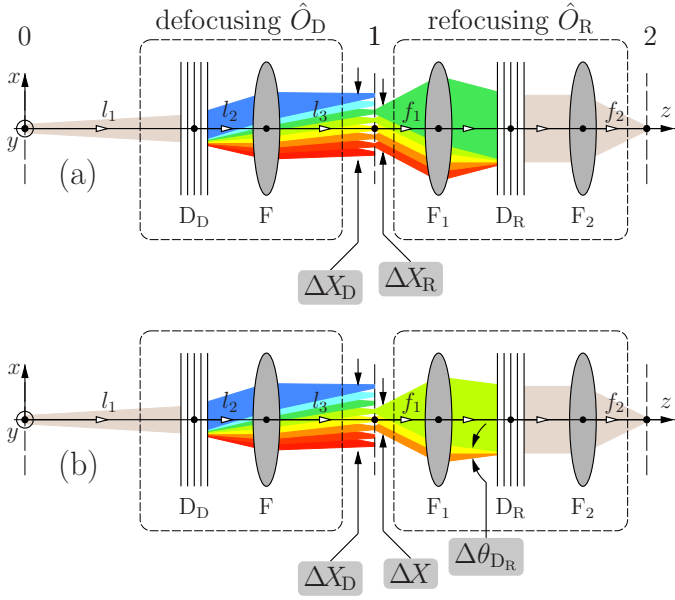


FIG. 8: Optical scheme of an x-ray echo spectrometer in the vertical scattering (dispersion) plane detailing the vertical beam size ΔX_D on the sample and the reduced effective vertical beam sizes ΔX_R and ΔX as seen by the refocusing system due to a smaller spectral bandwidth (a) or the limited angular acceptance $\Delta\theta_{D_R}$ (b).

10 meV for spectrometer XES1, and $\Delta X \simeq 105 \mu\text{m}$, $\Delta E = 2 \text{ meV}$ for spectrometer XES01.

If a smaller than ΔX vertical beam size on the sample is required, it can be always made by installing a beam-defining aperture in front of the sample. This will reduce proportionally the signal strength in the detector but leave intact the performance of the x-ray echo spectrometer in terms of spectral resolution and the spectral window of imaging. A better solution is obtained using an angular slit instead of the aperture, i.e., a Bragg reflecting crystal or a channel-cut crystal installed after dispersing element D_D , as was employed in [29].

VI. ECHO SPECTROMETER TOLERANCES

Permissible limits of variation of the echo spectrometer parameters can be calculated from the refocusing condition tolerance given by Eq. (7). The latter can be rewritten as

$$|G_D + G_R/A_R|\Delta E \ll \Delta x_1 \quad (25)$$

using Eq. (3) and the relationship $\Delta x_2 = |A_R|\Delta x_1$ from Eq. (4). The tolerance intervals can be defined more specifically by setting the requirement

$$|G_D + G_R/A_R|\Delta E \lesssim \nu \Delta x_1, \quad \nu \simeq 0.458, \quad (26)$$

that limits the blur of the image on the detector and therefore the degradation of the spectral resolution to 10%: $\sqrt{1 + \nu^2} = 1.1$.

In a particular case of the echo spectrometer, which has the optical scheme shown in Fig. 2, the tolerances on the spectrometer parameters can be calculated by

$$\left| \mathcal{D}_{U_D} \frac{l_3 l_1}{b_{U_D}^2 l_{12}} - \frac{\mathcal{D}_{U_R} f_1}{b_{U_R}} \right| \Delta E \lesssim \nu \Delta x_1, \quad (27)$$

which is obtained combining Eq. (26) and Eqs. (8)-(9). If the dispersing element D_D is placed from the source at a large distance $l_1 \gg b_{U_D}^2 l_2$, the tolerance equation in this case simplifies to

$$\left| \mathcal{D}_{U_D} l_3 - \frac{\mathcal{D}_{U_R} f_1}{b_{U_R}} \right| \Delta E \lesssim \nu \Delta x_1. \quad (28)$$

As an example, we assume that the spectrometer parameters are perfectly adjusted, except for the distance l_3 from the focusing optic to the secondary source (i.e., to the sample). The tolerance interval Δl_3 in this case can be estimated using Eq. (28) as

$$|\Delta l_3| \lesssim \nu \frac{\Delta x_1}{|\mathcal{D}_{U_D}| \Delta E}. \quad (29)$$

The focal length of the the collimating optic in practice may deviate from the design value f_1 due to uncertainties in fabrication. The tolerance interval Δf_1 can be estimated in this case as

$$|\Delta f_1| \lesssim \nu \frac{\Delta x_1 b_{U_R}}{|\mathcal{D}_{U_R}| \Delta E}. \quad (30)$$

With the parameters of the 0.1-meV-resolution echo spectrometer XES01, these tolerance intervals are estimated to be $|\Delta l_3| \lesssim 46 \text{ mm}$ and $|\Delta f_1| \lesssim 9 \text{ mm}$. For the 1-meV-resolution echo spectrometer XES1, they are $|\Delta l_3| \ll 91 \text{ mm}$ and $|\Delta f_1| \lesssim 9 \text{ mm}$. These requirements are not extremely demanding.

The variations in l_3 and f_1 can result from the sample position displacement, provided the sample is very thin, or from a sample having elongation along the beam and substantial scattering length of x-rays in the sample, or from uneven sample shape. Therefore, the above estimated numbers also provide constraints on the scattering length in the sample and the sample shape and size.

The spectral window of imaging can be technically shifted by varying the glancing angle of incidence (Bragg angle) of the D-crystal(s) in the dispersing element of the defocusing system, as discussed in Sec. VIII. Such variations, however, simultaneously change the dispersion rate \mathcal{D}_{U_D} of the defocusing system. How much \mathcal{D}_{U_D} can be changed without substantial violation of the refocusing condition? From Eq. (28) we find that the tolerance interval in this case is equal to

$$|\Delta \mathcal{D}_{U_D}| \lesssim \nu \frac{\Delta x_1}{l_3 \Delta E}. \quad (31)$$

With the parameters of the 0.1-meV-resolution echo spectrometer XES01, we obtain that $|\Delta \mathcal{D}_{U_D}| \lesssim$

0.64 $\mu\text{rad}/\text{meV}$. For the 1-meV-resolution XES1 spectrometer, $|\Delta\mathcal{D}_{\cup_D}| \ll 0.18 \mu\text{rad}/\text{meV}$. The permissible shifts of the spectral window of imaging will be discussed in Sec. VIII using these tolerance intervals.

If the spectrometer parameters are outside the tolerance intervals defined by Eqs. (29)–(31), the refocusing condition should be adjusted, as described in the following Sec. VII.

VII. REFOCUSING CONDITION ADJUSTMENT

The optical elements of the echo spectrometer have to be manufactured with a high accuracy so that the dispersion rates $\mathcal{D}_{\cup_D}, \mathcal{D}_{\cup_R}$, the asymmetry parameters b_{\cup_D}, b_{\cup_R} , and the focal distances f, f_1 are within the tolerance intervals defined by the refocusing condition Eq. (27). This, however, may not always be possible in practice. To overcome this problem, the refocusing condition can be exactly matched by adjusting the distances l_1, l_2 , and l_3 in the defocusing system (see Fig. 2) leaving all other parameters of the defocusing and refocusing systems intact. Given that the source-to-sample distance $l = l_1 + l_2 + l_3$, as well as the focal distance $f = l_{12}l_3/(l_{12} + l_3)$, and crystal parameters are fixed, the distances l_1, l_2 , and l_3 are defined from the above mentioned constraints, by solving the equations

$$l_1 + l_2 + l_3 = l \quad (32)$$

$$\frac{l_1}{b_{\cup_D}^2} + l_2 = \frac{fl_3}{l_3 - f}, \quad (33)$$

together with the refocusing condition given by Eq. (10). The solution of the system of Eqs. (10), (32), and (33) is

$$l_3 = \frac{l}{2} - \sqrt{\left(\frac{l}{2}\right)^2 - W\left(1 - \frac{1}{b_{\cup_D}^2}\right) - lf}, \quad (34)$$

$$l_1 = \frac{W}{l_3 - f}, \quad W = f_1 f \frac{\mathcal{D}_{\cup_R} b_{\cup_D}^2}{\mathcal{D}_{\cup_D} b_{\cup_R}}, \quad (35)$$

$$l_2 = \frac{l_3 f - W/b_{\cup_D}^2}{l_3 - f}. \quad (36)$$

Examples of distances l_3, l_2 , and l_1 calculated for slightly varying values of \mathcal{D}_{\cup_D} and b_{\cup_D} using Eqs. (34), (35), and (36) are shown in Tables III and IV for the cases of the 1-meV-resolution spectrometer XES1 and the 0.1-meV-resolution spectrometer XES01, respectively. Noteworthy, a small variation in \mathcal{D}_{\cup_D} and b_{\cup_D} results in a small variation of l_3 , but in a rather large variation of l_2 .

There is always a possibility of hitting the limit $l_2 = 0$, which, however, should be avoided in practice. This suggests the necessity of an iterative approach in the optical

| η_D | \mathcal{D}_{\cup_D} | b_{\cup_D} | l_3 | l_2 | l_1 | A_D |
|----------|------------------------------------|--------------|-------|-------|-------|---------|
| deg | $\frac{\mu\text{rad}}{\text{meV}}$ | | m | m | m | |
| 83.8 | 2.96 | 1.93 | 1.721 | 0.168 | 33.11 | -0.0984 |
| 84.0 | 3.11 | 1.98 | 1.725 | 0.609 | 32.66 | -0.0974 |
| 84.2 | 3.27 | 2.04 | 1.732 | 1.027 | 32.44 | -0.0967 |

TABLE III: Distances l_3, l_2 , and l_1 between the optical elements of the defocusing system calculated by Eqs. (34)–(36) for slightly different η_D and therefore \mathcal{D}_{\cup_D} and b_{\cup_D} values with $l = l_3 + l_2 + l_1 = 35$ m fixed. Other parameters are also fixed and given in Tables I and V. The 1-meV-resolution spectrometer XES1 is considered.

| η_D | \mathcal{D}_{\cup_D} | b_{\cup_D} | l_3 | l_2 | l_1 | A_D |
|----------|------------------------------------|--------------|-------|-------|--------|---------|
| deg | $\frac{\mu\text{rad}}{\text{meV}}$ | | m | m | m | |
| 77.5 | -29.86 | 1.9 | 1.710 | 0.197 | 33.092 | -0.0961 |
| 78 | -31.65 | 1.96 | 1.716 | 0.730 | 32.553 | -0.0951 |
| 79 | -35.92 | 2.08 | 1.722 | 1.731 | 31.546 | -0.0918 |

TABLE IV: Same as Table III, however for the 0.1-meV-resolution echo spectrometer XES01.

design of the x-ray echo spectrometers. In the first step, the initial values of the parameters entering W in Eq. (35) are determined from the required energy resolution and the refocusing condition, as in Section III. In the next step, W, l_3 , and l_2 are calculated from Eqs. (34)–(36). If l_2 is not positive, the crystal parameters \mathcal{D}_{\cup_D} and b_{\cup_D} of the defocusing dispersing element have to be adjusted to move l_2 into a comfortable range, e.g., $l_2 = 0.25$ m – 1 m. See examples presented in Tables III and IV.

VIII. SPECTRAL WINDOW OF IMAGING AND SCANNING RANGE

Unlike the conventional scanning-type narrow-band hard x-ray IXS spectrometers, x-ray echo spectrometers are imaging spectrographs. The spectral window of imaging, however, is limited and defined by the bandwidth ΔE_R of the refocusing system. How does one proceed if IXS spectra have to be imaged with an energy transfer ε outside the window of imaging? This can be accomplished by shifting the window of imaging into the region of interest. The practically simplest way is to shift the bandwidth ΔE_D of the defocusing system. Nothing has to be changed in the refocusing system \hat{O}_R , as illustrated in Fig. 9. Technically, the bandwidth of the defocusing system can be shifted either by varying the angle of incidence θ of the x-rays to the D-crystals of the dispersing elements, or by varying the crystal temperature and

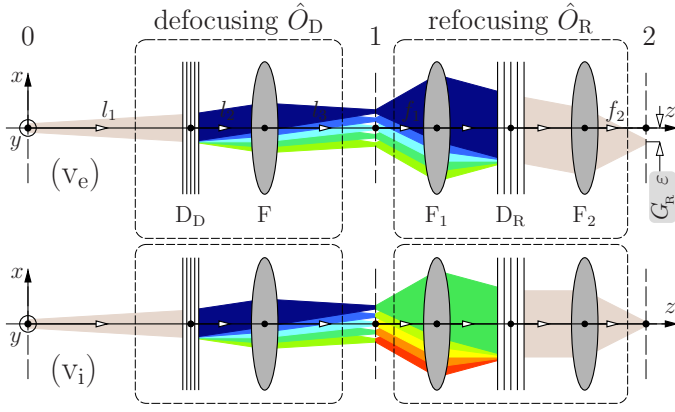


FIG. 9: Shifting the spectral window of imaging. A change in the crystal parameters in the dispersing element D_D of the defocusing system \hat{O}_D results in a change of the spectral composition of x-rays on the sample (compare with Fig. 2). Because the crystal parameters in the dispersing element D_R of the refocusing system \hat{O}_R are not changed, the elastically scattered photons are now refocused on the detector with a spatial shift (v_e). This results in a shift of the spectral imaging window. In particular, the inelastically scattered photons can now be refocused on the detector into the position which was associated before with elastically scattered photons (v_i).

therefore the crystal lattice parameter.³

It is important that the variation of the crystal parameters, e.g., the incidence angle θ of the dispersing element D_D , does not change the linear dispersion rate in the defocusing system \hat{O}_D over the limit $|\Delta\mathcal{D}_{U_D}|$ determined from Eq. (31), and therefore does not result in a violation of the refocusing condition. Otherwise, the refocusing condition has to be readjusted, as discussed in Sec. VII.

Let us determine how much of the bandwidth of the defocusing system can be shifted by varying the glancing angle of incidence θ without violation of the refocusing condition. The maximal spectral shift can be calculated apparently as

$$\delta E_{\max} = \pm \left| \frac{d\mathcal{D}_{U_D}}{d\theta} \frac{d\theta}{dE} \right|^{-1} |\Delta\mathcal{D}_{U_D}|. \quad (37)$$

In the simplest case of the dispersing element D_D consisting of one asymmetrically cut crystal, which is, e.g., the case of the 1-meV-resolution spectrometer XES1 (see Fig. 4) $\mathcal{D}_{U_D} = \mathcal{D}$ given by Eq. (13), and therefore we can calculate

$$\frac{d\mathcal{D}}{d\theta} \simeq -\frac{\mathcal{D}}{\theta - \eta}. \quad (38)$$

³ The spectral profile of the window of imaging can be measured by detecting the elastically scattered signal and scanning the bandwidth of the refocusing system in the similar way.

From Bragg's law, $d\theta/dE = -\tan\theta/E$. As a result,

$$\delta E_{\max} = \pm E \frac{\theta - \eta}{\tan\theta} \frac{|\Delta\mathcal{D}|}{|\mathcal{D}|}. \quad (39)$$

For the four-crystal CDDW-type dispersing element, the cumulative dispersion rate \mathcal{D}_{U_4} can be approximated to a good accuracy by Eq. (17). Assuming θ_3 is close to $\pi/2$ and $\theta_3 - \eta_3$ is small, the variation of \mathcal{D}_{U_4} with the glancing angles of incidence θ_2 and $\theta_3 = \theta_2$ in Bragg diffraction from the D-crystals crystals is given by

$$\frac{d\mathcal{D}_{U_4}}{d\theta_3} \simeq -\frac{2\mathcal{D}_{U_4}}{\theta_3 - \eta_3}, \quad (40)$$

an expression, which is similar to Eq. (38), differing only by factor 2.

It can be shown that for the CDDW optic, the variation of the bandwidth position with angle $dE/d\theta_3 \simeq -E/\tan\theta_3$ (in the approximation $\tan\theta_3 \gg \tan\theta_1$). Using this expression together with Eqs. (40) and (37), we obtain for the permissible shift of the spectral window of imaging of the CDDW-type dispersing element D_D :

$$\delta E_{\max} = \pm E \frac{\theta_3 - \eta_3}{2 \tan\theta_3} \frac{|\Delta\mathcal{D}_{U_4}|}{|\mathcal{D}_{U_4}|}. \quad (41)$$

To a factor of 1/2, it is equivalent to the one-crystal dispersing element case given by Eq. (39).

Using Eqs. (39) and (41), the tolerance interval values $|\Delta\mathcal{D}_{U_D}|$ calculated in Sec. VI for the 1-meV-resolution spectrometer XES1, and the 0.1-meV-resolution spectrometer XES01 together with the appropriate values of the dispersing element parameters from Tables I and II, respectively, we estimate for the permissible shift of the spectral window of imaging $\delta E_{\max} \simeq \pm 0.6$ eV for both spectrometers. The scanning ranges of the echo-type spectrometers are relatively large and comparable with those of the conventional scanning-type IXS spectrometers [8].

Since $|\delta E_{\max}|$ is much larger than the spectral window of imaging ΔE_R , the maximal energy transfer which can be measured, is $E_M \simeq |\delta E_{\max}|$. It is very important to note that $|\delta E_{\max}|$ and therefore E_M can be substantially increased, if the refocusing condition adjustment procedure is applied, as described in Sec. VII.

IX. IMPACT OF THE SECONDARY SOURCE SIZE ON THE SPECTRAL RESOLUTION

A. Vertical secondary source size

The vertical *monochromatic* secondary source size is determined by the vertical monochromatic focal spot size Δx_1 on the sample. We assume in the first approximation that they are equal and do not change with scattering angle Φ (see Fig. 2), provided the collimating optic and subsequent optical components of the refocusing system

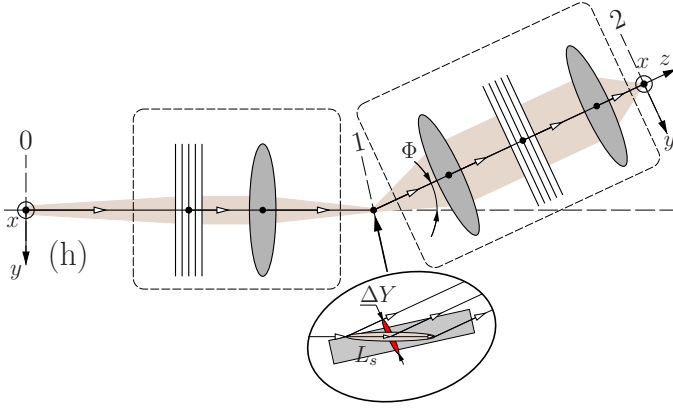


FIG. 10: Optical scheme of an x-ray echo spectrometer in the horizontal scattering plane, same as in Fig. 2(h), however, showing a close-up of the sample (gray rectangle) and the trace of the scattering path in the sample (pink ellipse), which details an increase of the secondary horizontal source size ΔY in the sample with scattering angle Φ .

are correctly aligned in the scattering plane. The smallness of Δx_1 and more precisely its angular size $\Delta x_1/f_1$ is critical for achieving high spectral resolution, given by Eq. (12).

B. Horizontal secondary source size

In contrast, the horizontal secondary source size ΔY changes with the scattering angle Φ (assuming the horizontal focal spot size is smaller). It increases with Φ as $\Delta Y \simeq L_s \sin \Phi$ because the projection of the scattering length L_s on the scattering direction increases; see pink ellipse in Fig. 10. To consider the impact of the horizontal size on the spectral resolution, we assume for simplicity in the following that the secondary source is concentrated in the sample reference plane 1, as indicated by the red ellipse in Fig. 10, i.e., there is no longitudinal component, and the secondary source distribution in reference plane 1 is presented by coordinates (x_1, y_1) . Such an approximation is well founded, because the spectral resolution is quite insensitive to the spread of the secondary source size along the optical axis, as discussed in Sec. VI.

X rays from secondary source point (x_1, y_1) propagate after the collimating optic F_1 at an angle $\varphi = y_1/f_1$ to the dispersion plane (x, z) . The glancing angle of incidence θ_1 to the Bragg reflecting atomic planes of the first crystal of the dispersing element D_R changes with φ to $\theta_{1\varphi}$, where

$$\sin \theta_{1\varphi} = \sin \theta_1 \cos \varphi. \quad (42)$$

In the approximation of a small φ , the angular difference

$$\theta_{1\varphi} - \theta_1 = -\xi_{1\varphi} = \frac{\varphi^2}{2} \tan \theta_1. \quad (43)$$

After n Bragg reflections (at the exit of the dispersing element D_R of the refocusing system), the vertical angular

difference $\xi'_{n\varphi}$ between the direction of x rays propagating in the dispersing plane and the direction of x-rays propagating with an angular deviation φ off the plane is

$$\xi'_{n\varphi} \simeq \Xi_n \xi_{1\varphi}. \quad (44)$$

The magnitude of Ξ_n in Eq. (44) depends on the concrete optical design of the dispersing element D_R . In the particular case of the four-crystal ($n = 4$) CDDW-type optic in the $(\pi+, \pi+, \pi-, 0-)$ scattering configuration presented in Figs. 6 and 7, Ξ_4 is given by

$$\Xi_4 \simeq -\frac{b_4(1 - b_3 b_2)}{\tan \theta_1 \cos \theta_2} \quad (45)$$

as shown in Appendix B. Here θ_2 is the nominal glancing angle of incidence to the reflecting atomic planes of the second crystal, which is assumed to be close to 90° and equal to θ_3 ; b_2, b_3 , and b_4 are the asymmetry factors of the Bragg reflections from the second, third, and fourth crystals, respectively.

We assume that the imaging optic F_2 , with a focal distance f_2 , focuses both vertically and horizontally. Each point of the secondary source with coordinates (x_1, y_1) in reference plane 1 will be imaged to a point (x_2, y_2) on the detector reference plane 2, where

$$x_2 = A_R x_1 + \xi'_{n\varphi} f_2, \quad y_2 = -y_1 \frac{f_2}{f_1}, \quad (46)$$

and $A_R = -b_{UR} f_2/f_1$ is the magnification factor of the refocusing system in the vertical dispersing plane; see Eq. (9). We note that in the horizontal non-dispersing plane, the magnification factor is just $-f_2/f_1$. Using Eqs. (43), (44), and (9), we obtain from Eq. (46)

$$x_2 = \left[x_1 + U \frac{\varphi^2}{2} \right] A_R, \quad y_2 = -y_1 \frac{f_2}{f_1} \quad (47)$$

where

$$U = \frac{f_1 \Xi_n \tan \theta_1}{b_{UR}}. \quad (48)$$

In the particular case of the CDDW-type optic, with Ξ_4 given by (45), we obtain

$$U = \frac{f_1(1 - b_3 b_2)}{|b_1 b_2 b_3| \cos \theta_2}. \quad (49)$$

If the secondary source size has a rectangular shape in reference (sample) plane 1 with a height Δx_1 and a width ΔY , its image, according to Eq. (47), acquires a curved shape; see Fig. 11. This result is in agreement with numeric simulations performed in [32] for the particular case of the x-ray echo spectrometer with designed parameters given in [1].

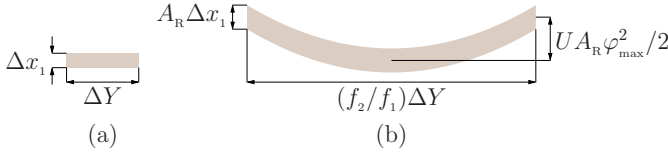


FIG. 11: The secondary monochromatic source of a rectangular shape in reference (sample) plane 1 (a) being imaged onto reference (detector) plane 2 acquires a curved shape (b) [see Eq. (47)] with $\varphi_{\max} = \Delta Y/2f_1$.

1. Curved image flattening

If a 2D-pixel detector is used to record the image, and if U is known, the curved shape can be reduced numerically to a flat one. U can be determined experimentally from the curvature of the elastic scattering image. With the curved image reduced to a flat one, the vertical size reduces to $\Delta x_2 = A_R \Delta x_1$, i.e., to a value unaffected by the horizontal source size. Therefore, if the flattening procedure is applied, the horizontal source size in the first approximation *does not deteriorate the spectral resolution* of the x-ray echo spectrometer.

2. Curved image

In contrast, if a 1D-pixel detector is used, sensitive in the x direction and integrating in the y direction, the vertical image size Δx_2 increases to

$$\Delta x_2 = |A_R| \sqrt{\Delta x_1^2 + \Delta x_{1\varphi}^2} \quad (50)$$

$$\Delta x_{1\varphi} = U \sqrt{\left\langle \left(\frac{\varphi^2}{2} \right)^2 \right\rangle} = \frac{U \varphi_{\max}^2}{2\sqrt{5}} = \frac{U \Delta Y^2}{8\sqrt{5} f_1^2}, \quad (51)$$

where $\varphi_{\max} = \Delta Y/2f_1$.

The spectral resolution $\Delta\epsilon$ of the echo spectrometer scales with the vertical image size Δx_2 ; see Eq. (6). Because of the horizontal spread ΔY of the secondary source size, Δx_2 acquires an additional component $A_R \Delta x_{1\varphi}$, resulting in a total vertical source size of $A_R \sqrt{\Delta x_1^2 + \Delta x_{1\varphi}^2} \simeq A_R \Delta x_1 (1 + \nu)$, where $\nu \simeq \Delta x_{1\varphi}^2 / 2\Delta x_1^2$. For the spectral resolution not to deteriorate by more than ν , we require that $\Delta x_{1\varphi} \lesssim \sqrt{2\nu} \Delta x_1$. Combining this expression with Eq. (51), we obtain for the permissible horizontal secondary source size:

$$\Delta Y \lesssim v \sqrt{\frac{8f_1^2 \Delta x_1}{U}}, \quad v = (10\nu)^{1/4}. \quad (52)$$

With U defined in Eq. (48),

$$\Delta Y \lesssim v \sqrt{\frac{8f_1 b_U \Delta x_1}{\Xi_n \tan \theta_1}} \quad (53)$$

in a general case, or with U defined in Eq. (49),

$$\Delta Y \lesssim v \sqrt{8f_1 \Delta x_1 |b_1 b_2 b_3| \cos \theta_2 / (1 - b_2 b_3)} \quad (54)$$

for the case of the CDDW optic.

For our exemplary echo-type IXS spectrometers (see Tables I, II, and V), we estimate $\Delta Y \lesssim 105 \mu\text{m}$ ($\varphi_{\max} = 260 \mu\text{rad}$; $U = 147 \text{ m}$) for 1-meV-resolution spectrometer XES1 and $\Delta Y \lesssim 320 \mu\text{m}$ ($\varphi_{\max} = 400 \mu\text{rad}$; $U = 60 \text{ m}$) for 0.1-meV-resolution spectrometer XES01, assuming a 10% limit ($\nu = 0.1$ and $v = 1$) of the spectral resolution degradation. The larger value of ΔY in case of spectrometer XES01 is due to a twice larger value of f_1 .

X. FOCUSING OPTICS

Focusing optics is another group of key elements of the x-ray echo spectrometer. A distinctive feature of the echo-type spectrometers is the propagation of different spectral components at different sometimes large angles to the optical axis; see Fig. 2. The angular deviation from the optical axis can be as large as $\pm \Delta \theta'_R / 2 \simeq \pm 150 \mu\text{rad}$ (see Tables I, II, and V) and may result in coma aberrations, and therefore degradation of the spectral resolution. It is essential that the focusing (F), collimating (F_1), and imaging (F_2) optical elements of the echo spectrometer, are capable of producing sharp images both with on-axis as well as off-axis illumination, i.e., they should be truly aberration-free imaging optical elements.

X-ray compound-refractive parabolic lenses (CRL) are genuine imaging devices [33] and are appropriate for x-ray echo spectrometers. However, because of the large photo absorption and therefore small, typically less than 1 mm effective apertures, their application is limited perhaps to the focusing element F of the defocusing system.

Grazing incidence curved mirrors have higher efficiency and therefore seem to be a preferred choice, especially for collimating (F_1) and imaging (F_2) optical elements. In the first approximation, they may have 2D paraboloidal shapes. Such mirrors are becoming available now [34]. Alternatively, more traditional systems comprised of two 1D parabolic mirrors mounted at 90° to each other can be used as well. Kirkpatrick-Baez (KB) mirrors [35] are arranged in-line one after the other, while Montel mirrors [36] are mounted side by side. Montel optics are especially attractive when the focal distance is comparable with the mirror length, which is the case for collimating elements F_1 .

Grazing incidence paraboloidal (parabolic) mirrors can focus x-ray beams properly, but only those propagating parallel to the parabola axis. A parallel beam with a lateral size B propagating at an angular deviation ξ from the axis is focused to a spot enlarged due to coma to a

size of ⁴

$$w = B |\xi|/\gamma, \quad (55)$$

and shifted by $x = \xi f$ from the optical axis. Here γ is nominal grazing incidence angle and f is the mirror's focal length. To prevent spectral resolution degradation, it is essential that coma $w \ll \Delta x_i$, i.e., much smaller than the perfect monochromatic image size Δx_i on the sample ($i = 1$) and on the detector ($i = 2$).

Typically, $\gamma \simeq 3$ mrad for grazing incidence mirrors designed for $\simeq 9$ keV x rays. For our exemplary echo-type IXS spectrometers (see Table V) $|\xi| \lesssim 150 \mu\text{rad}$ and $B \gtrsim 1$ mm. Thus, coma can enlarge the focal spots to $w \simeq 50 \mu\text{m}$ and more, i.e., to sizes which are more or much more than Δx_i . Therefore, grazing incidence parabolic mirrors as they are cannot be used as focusing optics of x-ray echo spectrometers.

A. Mitigating coma

Coma w of a paraboloidal mirror, Eq. (55), can be mitigated if the incidence angle γ can be enlarged and the incident x-ray's beam size B can be reduced. The angle γ can be enlarged by an order of magnitude and w reduced by the same amount, if one employs graded multilayer mirrors. Indeed, state-of-the-art commercially available high-reflectivity ($\simeq 70\%$) Mo/B₄C graded-multilayer mirrors designed for 9-keV photons may feature $\gamma \simeq 30$ mrad [37]. Additionally, in the particular case of mirror F₂, the problem can be mitigated further by increasing the focal distance f_2 , which is yet a free parameter, and therefore by increasing Δx_2 ; see Eqs. (4) and (9). Let us verify that this may work in the particular cases of the exemplary spectrometers.

Imaging mirror F₂. The imaging element F₂ in the refocusing dispersing system \hat{O}_R focuses x-rays onto the detector. Because the vertical beam size after the dispersing element D_R can be as large as $B = B_R/b_{\cup_R} = 3.5$ mm (see Table V) the imaging element F₂ has to have as large vertical geometrical aperture A_{2g} . Paraboloidal mirrors with graded multilayer coatings and a large incidence angle $\gamma \simeq 30$ mrad may feature sufficient geometrical aperture, relatively small length $\simeq A_{2g}/\gamma$, and relatively small coma $w < \Delta x_2$.

Indeed, we estimate $w = 14 \mu\text{m}$, for the case of the 1-meV-resolution spectrometer XES1, assuming $|\xi| = \pm \Delta\theta'_R/2 = \pm 0.12$ mrad and the above mentioned values of γ and B . For the 0.1-meV-resolution XES01 spectrometer with $B = B_R/b_{\cup_R} = 0.5$ mm, we obtain $w = 2.3 \mu\text{m}$. The estimated w -values are a factor of two to three smaller than the appropriate monochromatic image sizes Δx_2 given in Table V. Therefore, coma may de-

grade the spectral resolution in these cases by less than 10%.

Collimating mirror F₁. The collimating element F₁ in the refocusing dispersing system \hat{O}_R collects photons in a large solid angle $\Omega_h \times \Omega_v$, with $\Omega_h \simeq \Omega_v \simeq 1 - 10$ mrad (depending on the required momentum transfer resolution $\Delta Q \simeq K\Omega_h$), and makes parallel x-ray beams of each spectral component (assuming point secondary source). Laterally graded multilayer Montel mirrors proved to be useful exactly in this role [26, 38].

The impact of the coma aberration in collimating mirror F₁ on the spectral resolution of the echo-spectrometer $\Delta\varepsilon = |A_R|\Delta x_1/|G_R|$ [Eq. (6)] can be estimated by propagating parallel monochromatic beams in the opposite direction and calculating the effective increase of the ideal monochromatic secondary source size Δx_1 due to coma w , given by Eq. (55).

In particular, for the XES1 spectrometer with $f_1 = 0.2$ m, $\xi \simeq \Delta X/2f_1 = 0.125$ mrad, assuming a lateral size of the monochromatic collimated beam $B = B_R = 1$ mm and a grazing incidence angle $\gamma = 30$ mrad, we obtain $w = 4.1 \mu\text{m}$. Such coma increases by 30% the effective monochromatic secondary source size from $\Delta x_1 = 5 \mu\text{m}$ to an effective value of $\sqrt{\Delta x_1^2 + w^2}$, resulting also in a 30% degradation of the spectral resolution.

For the XES01 spectrometer, with $f_1 = 0.4$ m, $\xi \simeq \Delta X/2f_1 = 0.125$ mrad, and $B = B_R = 0.5$ mm (0.06 nm^{-1} resolution), we obtain $w = 2.1 \mu\text{m}$. Such broadening (coma) results in an 8% degradation of the spectral resolution.

The above examples demonstrate that increasing the incidence angle γ may substantially reduce coma.

B. Aberration-free optics

Single-reflection mirrors like grazing incidence paraboloidal mirrors suffer from coma, preventing true imaging, as already discussed in the previous section. Aberration-free imaging of an extended source or imaging over some extended field, involving off-axis mirror illumination, requires at least two reflections from two reflecting surfaces which exactly obey the Abbe sine condition [39–41].

Wolter optics, comprised of two grazing incidence mirrors, is able to create an x-ray imaging system with a relatively wide field of view [42]. Wolter systems typically consist of a paraboloidal primary mirror and a hyperboloidal or ellipsoidal secondary mirror. Wolter optics still may suffer from coma aberrations. To eliminate coma completely, small corrections are required to the mirror profile from their nominal second-order shape [43].

Combined KB-Wolter systems were proposed [44] and realized [45] for applications at synchrotron and x-ray free-electron laser sources. More advanced systems are under consideration [46] for full-field spectroscopy applications. Such KB-Wolter systems can be used as the

⁴ Xianbo Shi (APS) private communication.

aberration-free focusing element F of the defocusing system of the x-ray echo spectrometers.

The refocusing system already comprises two mirrors for collimation and imaging the secondary source on the detector. The idea suggests itself, whether such a two-mirror system could be an aberration-free Wolter-type one? Such a possibility was already considered by Howells with regard to soft x-ray plane grating monochromators [47], spectroscopic instruments with an optical scheme very similar to the discussed here scheme of the refocusing system of the echo spectrometer. Unlike the original proposal of Wolter, Howells suggested a double-mirror system in a parabola-parabola configuration. Such a configuration has the great advantage of producing parallel x-rays between the two reflections at the parabolas, see Figs. 12 and 13, which is perfect for the proper performance of a plane diffraction grating inserted between the collimating and focusing mirrors in the monochromator scheme. The parallel rays between the collimating and focusing mirrors in the parabola-parabola configuration is also perfect for the CDDW-type “plane diffraction gratings” considered in the present paper for the x-ray echo spectrometers.

In Appendix C, we show that the Abbe sine condition is satisfied exactly for a system with two identical parabolas producing one-to-one imaging. In a more general case of a system with two arbitrary parabolas, the sine condition may be satisfied to a very good accuracy, in particular, in cases of interest for x-ray echo spectrometer applications.

It should be noted, however, that because the CDDW dispersing crystal element changes the cross-section of the x-ray beam from B_R to B_R/b_{UR} , the 1:1 imaging with magnification factor $|A_R| = 1$ takes place if the focal distance of the imaging mirror $f_2 = f_1/b_{UR}$, see Eq. (9), differs from the focal distance of the collimating mirror f_1 by a factor of $1/b_{UR}$. In other words, the identical parabolas, ensuring perfect imaging obeying Abbe sine condition under these conditions, cannot be actually identical. The focal distance and the size of the second mirror should be scaled by a factor of $1/b_{UR}$ as the beam cross-section, see Fig. 12.

XI. PIXEL DETECTORS AND SPECTRAL RESOLUTION OF ECHO SPECTROMETERS

The monochromatic image size Δx_2 on the pixel detector determines the required spatial resolution of the detector, which should be $\Delta x_D \ll \Delta x_2$, to not deteriorate the echo spectrometer spectral resolution $\Delta\varepsilon = \Delta x_2/|G_R|$, see Eq. (6). If the spatial resolution of the detector cannot be neglected, i.e., $\Delta x_D \gtrsim \Delta x_2$, the spectral resolution degrades to

$$\Delta\varepsilon = \sqrt{(\Delta x_2)^2 + (\Delta x_D)^2}/|G_R|. \quad (56)$$

In the particular case of the echo spectrometer with the optical scheme presented in Sec. III and in Fig. 2, the

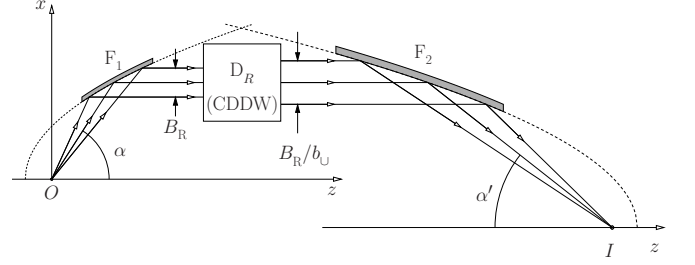


FIG. 12: Optical scheme of the refocusing system of the x-ray echo spectrometer, see Fig. 2, here shown comprising parabolic collimating mirror F_1 , parabolic imaging mirror F_2 , and dispersing element D_R (CDDW-type four-crystal system - Figs. 7-6) in between. The Abbe sine condition is fulfilled exactly ($\sin \alpha / \sin \alpha' = 1$) in the case of one-to-one imaging, which takes place if the focal distances of the mirrors are related as $f_2 = f_1/b_{UR}$. Here $f_1 = OF_1$, $f_2 = IF_2$.

spectral resolution given by Eq. (12) is transformed using Eq. (56) to

$$\Delta\varepsilon = \frac{|b_{UR}|}{|D_{UR}|} \frac{\Delta x_1}{f_1} \sqrt{1 + \left(\frac{1}{|b_{UR}|} \frac{\Delta x_D f_1}{\Delta x_1 f_2} \right)^2}. \quad (57)$$

Equation (57) indicates that a large f_2 is beneficial for diminishing the negative impact of the limited spatial resolution. If a less than 10% spectral resolution degradation is permissible, we estimate from Eq. (57) for the required detector spatial resolution: $\Delta x_D = 15 \mu\text{m}$ and $\Delta x_D = 3 \mu\text{m}$ for our exemplary echo-type IXS spectrometers XES1 and XES01, respectively (see parameters in Table V). Appropriate for this application, x-ray photon-counting detectors with $\Delta x_D = 2 \mu\text{m}$ are state of the art [48, 49].

XII. DISCUSSION AND CONCLUSIONS

Hard x-ray echo spectroscopy, a space-domain counterpart of neutron spin echo, was recently introduced [1] to overcome limitations in the spectral resolution and weak signals of the traditional narrow-band scanning IXS probes. X-ray echo spectroscopy relies on imaging IXS spectra, and does not require x-ray monochromatization. Due to this, the echo-type IXS spectrometers are broad band and have a potential to simultaneously provide dramatically increased signal strength, reduced measurement times, and higher resolution compared to the traditional narrow-band scanning-type IXS spectrometers. The main components of the x-ray echo spectrometer are defocusing and refocusing systems, comprised of dispersing and focusing elements.

The theory of the x-ray echo spectrometers presented in [1] is developed here further with a focus on questions of practical importance, which could facilitate optical design and assessment of the feasibility and performance of

| Spectrometer: | XES1 | XES01 | HERIX |
|---|--------------------|---------------|----------|
| Parameter: | | | |
| Photon energy E [keV] | 9.137 | 9.137 | 23.74 |
| Photon momentum K [nm ⁻¹] | 46.3 | 46.3 | 120.3 |
| Spectral resolution $\Delta\varepsilon$ [meV] | 1 | 0.1 | 1.5 |
| Momentum transfer resolution ΔQ [nm ⁻¹] | 0.46 | 0.05 | 1.2 |
| Angular acceptance $\Omega_v \times \Omega_h$ [mrad ²] | 10×10 | 1.1×1.1 | 10×10 |
| Effective bandwidth ΔE [meV] | 10 | 2 | 1 |
| Spectral window of imaging ΔE_R [meV] | 14.2 | 8.0 | 1 |
| Max. energy transfer E_M [eV] ^a | 0.6 | 0.6 | 10 |
| Max. scattering angle Φ_M | 154° | 154° | 35° |
| Max. momentum transfer Q_M [nm ⁻¹] | 90 | 90 | 70 |
| Analyzer arm length [m] | 2 | 3.5 | 9 |
| Incident photon polarization | π | π | σ |
| Effective vertical beam size on the sample ΔX [μ m] | 50 | 100 | 20 |
| Permissible horizontal secondary sources size ΔY [μ m] ^b | 105 | 320 | 1000 |
| Cumulative \mathcal{D}_{\cup_D} of D_D [μ rad/meV] | -3.12 | -31.7 | - |
| Cumulative b_{\cup_R} of D_R | 0.65 | 0.27 | - |
| Cumulative $\mathcal{D}_{\cup_R}/b_{\cup_R}$ of D_R [μ rad/meV] | -25 | -125 | - |
| Angular acceptance $\Delta\theta_R$ of D_R [μ rad] | 246 | 262 | - |
| Angular divergence $\Delta\theta'_R = \Delta E_R \mathcal{D}_{\cup_R} $ after D_R [μ rad] | 234 | 272 | - |
| Vertical beam size B_R on D_R [mm] | 2 | 0.43 | - |
| Vertical beam size B_R/b_{\cup_R} after D_R [mm] | 3.5 | 1.6 | - |
| Focusing mirror focal length f [m] | 1.446 ^c | 1.446 | 1.5 |
| Collimating mirror focal length f_1 [m] | 0.2 | 0.4 | - |
| Imaging mirror focal length f_2 [m] | 2 | 2 | - |
| Smallest image size Δx_2 on the pixel detector [μ m] | 32 | 6.8 | - |
| Spectral flux F ^d [ph/meV/s] $\times 10^{10}$ | 30 | 30 | 4.2 |
| Relative signal strength S/S^{HERIX} | 1014× ζ | 1.3 × ζ | 1 |

^aCan be substantially increased if the adjustment procedure of the refocusing condition is applied; see Sec. VII.

^bCan be substantially increased by curved image flattening procedure; see Sec. IX B 1.

^cA CRL comprised of 17 double-convex Be lenses with $R = 200 \mu\text{m}$.

^dAs predicted for the standard undulator of the upgraded Advanced Photon Source [50].

TABLE V: Operation parameters and performance characteristics of the considered exemplary echo spectrometers XES1 and XES01 compared with the parameters of the state-of-the-art narrow-band scanning IXS spectrometer HERIX [10, 11]. The signal strength is $S \propto \Delta E \times \Delta E_R \times \Omega_v \times \Omega_h \times F \times L_s$, where L_s is the scattering length. The relative signal strength values in the bottom row have to be corrected for each particular sample using $\zeta = L_s/L_s^{\text{HERIX}}$. The scattering length L_s is given either by the absorption length L_a or by the sample thickness, if it is smaller. Typically $L_a/L_a^{\text{HERIX}} \simeq 1/2 - 1/30$. A *monochromatic* focal spot size of $\Delta x_1 = 5 \mu\text{m}$ on the sample is assumed in all cases.

echo spectrometers. Among others, the following questions are addressed: spectral resolution, refocusing condition, echo spectrometers tolerances, refocusing condition adjustment, effective beam size on the sample, spectral window of imaging and scanning range, the impact of secondary source size on the spectral resolution, the angular dispersive optics, the focusing and collimating optics, etc.

The analytical ray-transfer matrix (ray-tracing) approach is used to calculate spectral resolution, refocusing condition, echo spectrometers tolerances, etc. Spec-

tral bandwidth and efficiency of the dispersing elements are calculated using dynamical diffraction theory of x-ray Bragg diffraction in crystals.

The developed theory provides recommendations on the optical design of the x-ray echo spectrometer and on the design procedure. In particular, the equations defining the spectral resolution and the refocusing condition can be used for the initial estimation of the dispersion rates required for the dispersing elements, which in turn determine the possible optical design of the dispers-

ing elements. Four-crystal CDDW-type arrangements of asymmetrically cut crystals are proposed as large-dispersion-rate dispersing elements. The optical parameters of the x-ray echo spectrometers can be further specified more precisely by refining the refocusing condition. The refocusing condition is also essential for the calculation of the echo spectrometer tolerances. If the dispersion rate of a dispersing element, or the focal length of a focusing element deviates from its design value, the refocusing condition can be tuned by adjusting the distances between the optical elements of the defocusing system. This procedure is very useful, in particular, for extending the spectral scanning range from a fraction of eV to a few eVs. Another important recommendation of the theory is to apply the numerical procedure of flattening the curved image on the detector, and thus to eliminate the detrimental influence of the horizontal secondary source on the spectral resolution.

Examples of optical designs and characteristics of echo spectrometers with 1-meV and 0.1-meV resolutions are discussed in the paper supported by the theory. The theory is used to calculate the operation and performance characteristics of the exemplary x-ray echo spectrometers, which are summarized in Table V. These are compared with what is possible with the state-of-the-art narrow-band scanning-type IXS spectrometers [8], in particular with HERIX, a 1.5-meV-resolution IXS spectrometer at the Advanced Photon Source (APS) [10, 11]. The signal of the 1-meV-resolution echo-type spectrometer XES1 is enhanced by three orders of magnitude compared to HERIX, provided the scattering length in the sample is the same; see Table V for more details. The momentum resolution is three times better for the same solid angle of collection of scattered photons. The signal strength of the 0.1-meV-resolution echo-type spectrometer XES01 is comparable to that of the 1-meV-resolution HERIX spectrometer. Importantly, not only the spectral resolution is improved by an order of magnitude, the momentum transfer resolution of XES01 is also improved compared to HERIX by a factor of 25 (from 1.2 nm^{-1} to 0.05 nm^{-1}). That means that IXS experiments with an order of magnitude improved spectral and momentum transfer resolutions are becoming feasible at storage-ring-based x-ray sources by applying the x-ray echo spectroscopy approach.

The point is that an even higher spectral resolution $\Delta\varepsilon \lesssim 0.02 \text{ meV}$ and momentum transfer resolution can be achieved with x-ray echo spectrometers by increasing the dispersion rates \mathcal{D}_U in the dispersing elements. This, however, will result in their narrower transmission bandwidths ΔE_U . Still, an approximately constant ratio $\Delta E_U/\Delta\varepsilon$ will hold. Alternatively, the spectral resolution can be improved by increasing the focal length f_1 of the collimating optic F_1 , or by reducing the secondary source size Δx_1 (by improving focusing on the sample); see Eq. (12). The signal strength will drop. However, high-repetition-rate self-seeded x-ray free-electron lasers will provide in the future orders of magnitude more spec-

tral flux than what is possible at storage ring sources [9], and therefore will make feasible experiments with an extremely high spectral resolution $\Delta\varepsilon \lesssim 0.01 \text{ meV}$.

It is essential that the focusing (F), collimating (F_1), and imaging (F_2) optical elements of the x-ray echo spectrometer are capable of producing sharp images both with on-axis as well as off-axis illumination, i.e., they should be truly aberration-free imaging optical elements. The spectral resolution and spectral line shape will largely depend on the quality of the focusing, collimating, and imaging optical elements.

The magnitude of the image Δx_2 on the pixel detector defines the required spatial resolution, which is in the $15\text{-}\mu\text{m}$ to $3\text{-}\mu\text{m}$ range, depending on the spectrometer. Detectors with such spatial resolution are state of the art [48, 49].

X-ray echo spectrometers require a combination of CDDW dispersing elements and focusing optics as major optical components. Such components have been experimentally demonstrated recently [26, 29]. Implementation of x-ray echo spectrometers is, therefore, realistic.

XIII. ACKNOWLEDGMENTS

Lahsen Assoufid, Patricia Fernandez, Jonathan Lang, and Stephan Streiffer (APS) are acknowledged for supporting the project. Xianbo Shi (APS) is acknowledged for valuable discussions of aberrations in x-ray parabolic mirrors. Work at Argonne National Laboratory was supported by the U.S. Department of Energy, Office of Science, under Contract No. DE-AC02-06CH11357.

Appendix A: Ray-transfer matrices

Ray-transfer matrices $\{A0G, CDF, 001\}$ of the defocusing \hat{O}_D and refocusing \hat{O}_R systems of the x-ray echo spectrometers used in the paper are given in the last two rows of Table VI. They are equivalent to the ray-transfer matrices of x-ray focusing monochromators and spectrographs derived in Ref. [27]. The matrices of the multi-element systems \hat{O}_D and \hat{O}_R are obtained by successive multiplication of the matrices of the constituent optical elements, which are given in the upper rows of Table VI.

In the first three rows, 1–3, matrices are shown for the basic optical elements, such as propagation in free space $\hat{P}(l)$, thin lens or focusing mirror $\hat{L}(f)$, and Bragg reflection from a crystal $\hat{C}(b, sD)$. Scattering geometries in Bragg diffraction from crystals are defined in Fig. 3. In the following rows of Table VI, ray-transfer matrices are shown for arrangements composed of several basic optical elements, such as successive multiple Bragg reflections from crystals $\hat{C}(b_{U_n}, \mathcal{D}_{U_n})$ and $\hat{K}(b_{U_n}, \mathcal{D}_{U_n}, l)$, rows 4–5; and a focusing system $\hat{F}(l_2, f, l_1)$, row 6.

The matrices of the defocusing \hat{O}_D and refocusing

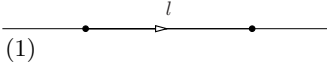
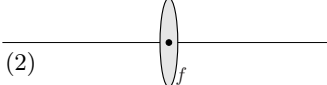
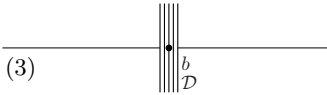
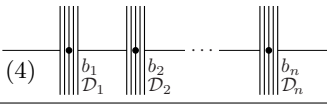
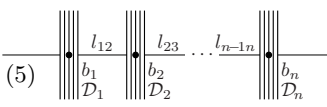
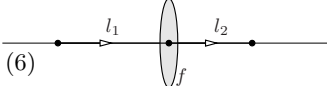
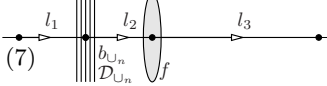
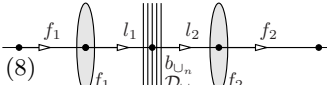
| Optical system | Matrix notation | Ray-transfer matrix | Definitions and remarks |
|---|--|--|--|
| Free space [12, 14]  (1) | $\hat{P}(l)$ | $\begin{pmatrix} 1 & l & 0 \\ 0 & 1 & 0 \\ 0 & 0 & 1 \end{pmatrix}$ | l – distance |
| Thin lens [12, 14]  (2) | $\hat{L}(f)$ | $\begin{pmatrix} 1 & 0 & 0 \\ -\frac{1}{f} & 1 & 0 \\ 0 & 0 & 1 \end{pmatrix}$ | f – focal length |
| Bragg reflection from a crystal [13, 28]  (3) | $\hat{C}(b, s\mathcal{D})$ | $\begin{pmatrix} 1/b & 0 & 0 \\ 0 & b & s\mathcal{D} \\ 0 & 0 & 1 \end{pmatrix}$ | $b = -\frac{\sin(\theta+\eta)}{\sin(\theta-\eta)}$ asymmetry factor; $\mathcal{D} = -(1/E)(1+b)\tan\theta$ angular dispersion rate. |
| Successive Bragg reflections [27] $\hat{C}(b_n, s_n \mathcal{D}_n) \cdots \hat{C}(b_1, s_1 \mathcal{D}_1)$  (4) | $\hat{C}(b_{\cup_n}, \mathcal{D}_{\cup_n})$ | $\begin{pmatrix} 1/b_{\cup_n} & 0 & 0 \\ 0 & b_{\cup_n} & \mathcal{D}_{\cup_n} \\ 0 & 0 & 1 \end{pmatrix}$ | $b_{\cup_n} = b_1 b_2 b_3 \dots b_n$ $\mathcal{D}_{\cup_n} = b_n \mathcal{D}_{\cup_{n-1}} + s_n \mathcal{D}_n$ $s_i = \pm 1, i = 1, 2, \dots, n$ |
| Successive Bragg reflections with space between crystals [27] $\hat{C}(b_n, s_n \mathcal{D}_n) \cdots \hat{P}(l_{12}) \hat{C}(b_1, s_1 \mathcal{D}_1)$  (5) | $\hat{K}(b_{\cup_n}, \mathcal{D}_{\cup_n}, l)$ | $\begin{pmatrix} 1/b_{\cup_n} & B_{\cup_n} & G_{\cup_n} \\ 0 & b_{\cup_n} & \mathcal{D}_{\cup_n} \\ 0 & 0 & 1 \end{pmatrix}$ | $B_{\cup_n} = \frac{B_{\cup_{n-1}} + b_{\cup_{n-1}} l_{n-1n}}{b_n}$ $G_{\cup_n} = \frac{G_{\cup_{n-1}} + \mathcal{D}_{\cup_{n-1}} l_{n-1n}}{b_n}$ $B_{\cup_1} = 0, \quad G_{\cup_1} = 0$ |
| Focusing system $\hat{P}(l_2) \hat{L}(f) \hat{P}(l_1)$  (6) | $\hat{F}(l_2, f, l_1)$ | $\begin{pmatrix} 1 - \frac{l_2}{f} & B_F & 0 \\ -\frac{1}{f} & 1 - \frac{l_1}{f} & 0 \\ 0 & 0 & 1 \end{pmatrix}$ | $B_F = l_1 l_2 \left(\frac{1}{l_1} + \frac{1}{l_2} - \frac{1}{f} \right)$ |
| Defocusing system \hat{O}_D [27] $\hat{F}(l_3, f, l_2) \hat{C}(b_{\cup_n}, \mathcal{D}_{\cup_n}) \hat{P}(l_1)$  (7) | \hat{O}_D | $\begin{pmatrix} \frac{1}{b_{\cup_n}} \left(1 - \frac{l_3}{f} \right) & 0 & X \mathcal{D}_{\cup_n} \\ -\frac{1}{f b_{\cup_n}} & b_{\cup_n} \left(1 - \frac{l_{12}}{f} \right) & \left(1 - \frac{l_2}{f} \right) \mathcal{D}_{\cup_n} \\ 0 & 0 & 1 \end{pmatrix}$ | $\frac{1}{l_{12}} + \frac{1}{l_3} = \frac{1}{f}$ $l_{12} = l_1 / b_{\cup_n}^2 + l_2$ $X = l_3 l_1 / (b_{\cup_n}^2 l_{12})$ |
| Refocusing system \hat{O}_R [27] $\hat{F}(f_2, f_2, l_2) \hat{C}(b_{\cup_n}, \mathcal{D}_{\cup_n}) \hat{F}(l_1, f_1, f_1)$  (8) | \hat{O}_R | $\begin{pmatrix} -\frac{b_{\cup_n} f_2}{f_1} & 0 & f_2 \mathcal{D}_{\cup_n} \\ \frac{(l_1 - f_1) + (l_2 - f_2) b_{\cup_n}^2}{b_{\cup_n} f_1 f_2} & -\frac{f_1}{b_{\cup_n} f_2} & \left(1 - \frac{l_2}{f_2} \right) \mathcal{D}_{\cup_n} \\ 0 & 0 & 1 \end{pmatrix}$ | |

TABLE VI: Ray-transfer matrices $\{ABG, CDF, 001\}$ of optical systems used in the paper. The matrices are shown starting with basic ones in rows 1–3. Matrices of combined systems are given in rows 4–6. The ray transfer matrices of the defocusing \hat{O}_D and refocusing \hat{O}_R systems of x-ray echo spectrometers are presented in rows 7–8. Definition of the glancing angle of incidence θ to the reflecting crystal atomic planes, the asymmetry angle η , and the deflection sign s in Bragg diffraction from a crystal, used for the Bragg reflection ray-transfer matrix in row 3, are given in Fig. 3. See Ref. [27] for more details.

\hat{O}_R systems presented in Table VI, rows 7 and 8, respectively, are calculated using the multi-crystal matrix $\hat{C}(b_{\cup_n}, \mathcal{D}_{\cup_n})$ from row 4, assuming zero free space between crystals in successive Bragg reflections. Generalization to a more realistic case of nonzero distances between the crystals requires the application of matrix $\hat{K}(b_{\cup_n}, \mathcal{D}_{\cup_n}, l)$ from row 5.

We refer to Ref. [27] for details on the derivation of these matrices. Here, we provide only the final results, notations, and definitions.

Appendix B: Derivation of Ξ_n

In Sec. IX B, we consider a linear secondary source in reference plane 1 extended in the horizontal scattering plane along the y -axis (perpendicular to the optical axis z); see Fig. 10. Each point of the linear secondary source radiates x-rays in 4π , but the collimating element F_1 captures them in a large solid angle and makes them propagate in parallel towards the dispersing element D_R . The rays propagate parallel to the plane (y, z) but at an angle φ to the dispersion plane of the first crystal, which is parallel to plane (x, z) in Fig. 10, and at an angle $\theta_{1\varphi}$ to the diffracting atomic planes of the first crystal; see Eq. (43). We will consider n successive Bragg reflections from n crystals, and will calculate the vertical angular difference $\xi'_{n\varphi}$ after the n -th reflection between the direction of x rays propagating in the dispersion plane ($\varphi = 0$) and the direction of x-rays propagating with an angular deviation φ off the plane. In particular, we will show that $\xi'_{n\varphi} \simeq \Xi_n \xi_{n\varphi}$ and derive the constant Ξ_n ; see Eq. (44).

For each crystal, we use here a local reference system $\{x'_n, y'_n, z'_n\}$, as defined in [24] (Fig. 2.4). We assume that the dispersion planes (x'_n, z'_n) of all crystals are parallel to each other (as well as the y'_n -axis). Wave-vectors of photons incident on and diffracted from the n -th crystal in this reference system can be presented by

$$\mathbf{K}_{n\varphi} = K \begin{pmatrix} \cos \theta_{n\varphi} \cos \phi_{n\varphi} \\ \cos \theta_{n\varphi} \sin \phi_{n\varphi} \\ -\sin \theta_{n\varphi} \end{pmatrix}, \quad \mathbf{K}'_{n\varphi} = K \begin{pmatrix} \cos \theta'_{n\varphi} \cos \phi'_{n\varphi} \\ \cos \theta'_{n\varphi} \sin \phi'_{n\varphi} \\ \sin \theta'_{n\varphi} \end{pmatrix}, \quad (\text{B1})$$

respectively. Here, $\theta_{n\varphi}$ is the glancing angle of incidence and $\theta'_{n\varphi}$ the glancing angle of reflection measured relative to the diffracting atomic planes parallel to (x'_n, y'_n) , while $\phi_{n\varphi}$ is the azimuthal angle of incidence and $\phi'_{n\varphi}$ is the azimuthal angle of reflection measured as a deviation from the dispersion plane.

The angular deviation φ relates to the azimuthal angle ϕ_1 by

$$\phi_{1\varphi} = \frac{\varphi}{\cos \theta_1}. \quad (\text{B2})$$

We assume that φ , $\phi'_{n\varphi}$, and $\phi_{n\varphi}$ are small for all crystals. It can be shown that under these conditions to a good accuracy

$$\phi'_{n\varphi} \simeq \phi_{n\varphi}. \quad (\text{B3})$$

Following the rule that the counterclockwise sense of angular variations of the ray slope ξ to the optical axis is positive (see Fig. 3 of [27] for more details) we define

$$\theta_{n\varphi} = \theta_n - s_n \xi_{n\varphi}, \quad \theta'_{n\varphi} = \theta'_n + s_n \xi'_{n\varphi}. \quad (\text{B4})$$

Here θ_n and θ'_n are the nominal ‘‘Bragg angles’’ of incidence and reflection, respectively, of x-rays with a particular photon energy propagating in the dispersion planes at $\varphi = 0$. The angular variations $\xi'_{n\varphi}$ and $\xi_{n\varphi}$ are related to each other by

$$\xi'_{n\varphi} = b_n \xi_{n\varphi}, \quad (\text{B5})$$

as follows from the Bragg reflection ray-transfer matrix $\hat{C}(b, s\mathcal{D})$ [see Table VI] assuming that a small deviation ϕ of x-rays from the dispersion plane does not violate it.

For all crystals to be in Bragg reflection, each successive crystal n has to be rotated by an angle

$$\alpha_n = \begin{cases} \theta'_{n-1} + \theta_n & \text{in } (++) \text{ or } (--) \text{ geometry} \\ \theta'_{n-1} - \theta_n + \pi & \text{in } (+-) \text{ or } (-+) \text{ geometry} \end{cases} \quad (\text{B6})$$

about the y'_n crystal axis, which is parallel to the y'_{n-1} axis of the previous $(n-1)$ -th crystal. The rotation matrix in this case is

$$\hat{R}(\alpha_n) = \begin{pmatrix} \cos \alpha_n & 0 & \sin \alpha_n \\ 0 & 1 & 0 \\ -\sin \alpha_n & 0 & \cos \alpha_n \end{pmatrix}. \quad (\text{B7})$$

The momentum of a photon reflected from the n -th crystal and incident on the $(n+1)$ -th crystal can be presented in the reference system $\{x'_n, y'_n, z'_n\}$ of the n -th crystal as $\mathbf{K}'_{n,\varphi}$ and as $\mathbf{K}_{n+1,\varphi}$ in the reference system $\{x'_{n+1}, y'_{n+1}, z'_{n+1}\}$ of the $(n+1)$ -th crystal, and related to each other by

$$\mathbf{K}_{n+1,\varphi} = \hat{R}(\alpha_{n+1}) \mathbf{K}'_{n\varphi}. \quad (\text{B8})$$

Using Eq. (B1) for $\mathbf{K}'_{n\varphi}$, and $\mathbf{K}_{n+1,\varphi}$ and equalizing vector components in Eq. (B8), we have

$$\cos \theta_{n+1,\varphi} \cos \phi_{n+1,\varphi} = \cos \theta'_{n\varphi} \cos \phi_{n\varphi} \cos \alpha_{n+1} + \sin \theta'_{n\varphi} \sin \alpha_{n+1}, \quad (\text{B9})$$

$$\cos \theta_{n+1,\varphi} \sin \phi_{n+1,\varphi} = \cos \theta'_{n\varphi} \sin \phi_{n\varphi}, \quad (\text{B10})$$

$$-\sin \theta_{n+1,\varphi} = -\cos \theta'_{n\varphi} \cos \phi_{n\varphi} \sin \alpha_{n+1} + \sin \theta'_{n\varphi} \cos \alpha_{n+1}. \quad (\text{B11})$$

Taking $\theta_{n+1,\varphi} = \theta_{n+1} - s_{n+1} \xi_{n+1,\varphi}$ from Eq. (B4) and the fact that $|\xi_{n+1,\varphi}| \ll 1$, we can present the left-hand side of Eq. (B11) as

$$-\sin \theta_{n+1,\varphi} \simeq -\sin \theta_{n+1} + s_{n+1} \xi_{n+1,\varphi} \cos \theta_{n+1}. \quad (\text{B12})$$

Using $\theta'_{n\varphi} = \theta'_n + s_n b_n \xi_{n\varphi}$ from Eqs. (B4)–(B5); the approximation $\cos \phi_{n\varphi} \simeq (1 - \phi_{n\varphi}^2/2)$; Eq. (B6); and omitting terms $\propto \phi^2 \xi$, we can present the right-hand side of Eq. (B11) as

$$\begin{aligned} & -\cos \theta'_{n\varphi} \cos \phi_{n\varphi} \sin \alpha_{n+1} \cos \phi_{n+1} + \sin \theta'_{n\varphi} \cos \alpha_{n+1} \\ & \simeq -\sin \theta_{n+1} + s_n b_n \xi_{n\varphi} \cos(\theta'_n - \alpha_{n+1}) + \frac{\phi_{n\varphi}^2}{2} \cos \theta'_n \sin \alpha_{n+1}. \end{aligned} \quad (\text{B13})$$

From Eq. (B6) we have

$$\cos(\alpha_{n+1} - \theta'_n) = S_{n+1,n} \cos \theta_{n+1} \quad (\text{B14})$$

where $S_{n+1,n} = +1$ in the $(++)$ or $S_{n+1,n} = -1$ in the $(+-)$ scattering geometry. Finally, using Eq. (B14) and inserting Eqs. (B12)–(B14) into Eq. (B11), we obtain a recursive relationship for $\xi_{n\varphi}$:

$$s_{n+1} \xi_{n+1,\varphi} = S_{n+1,n} b_n s_n \xi_{n\varphi} + \frac{\phi_{n\varphi}^2}{2} \frac{\cos \theta'_n}{\cos \theta_{n+1}} \sin \alpha_{n+1}. \quad (\text{B15})$$

A recursive relationship for $\phi_{n\varphi}$ is derived from Eq. (B10):

$$\phi_{n+1,\varphi} \simeq \frac{\cos \theta'_n}{\cos \theta_{n+1}} \phi_{n\varphi}. \quad (\text{B16})$$

Now, Ξ_n [see Eq. (44)] can be calculated using the above recursive relationships together with Eq. (B5).

Here, as an example, we will calculate Ξ_4 for the particular case of the four-crystal ($n = 4$) CDDW-type optic in the $(\pi+, \pi+, \pi-, 0-)$ scattering configuration presented in Figs. 6 and 7.

Taking $S_{2,1} = +1$, $s_1 = +1$, $\theta'_1 \simeq \theta_1$, $\sin \alpha_2 = \sin(\theta_2 + \theta'_1) \simeq \cos \theta_1$ (we assume that θ_2 is close to $\pi/2$ as is the case of the D-crystals $n = 2, 3$), and $\phi_{1\varphi}^2/2 = -\xi_{1\varphi}/(\sin \theta_1 \cos \theta_1)$ derived from Eqs. (43) and (B2), we have from Eq. (B15) that

$$s_2 \xi_{2\varphi} = b_1 \xi_{1\varphi} - \frac{\xi_{1\varphi}}{\tan \theta_1 \cos \theta_2}. \quad (\text{B17})$$

Because $|b_1| \ll 1$, $\tan \theta_1 \ll 1$, and $\cos \theta_2 \ll 1$, Eq. (B17) approximates to

$$s_2 \xi_{2\varphi} \simeq -\frac{\xi_{1\varphi}}{\tan \theta_1 \cos \theta_2}. \quad (\text{B18})$$

Further, taking $S_{3,2} = -1$, $\theta'_2 \simeq \theta_3$, and $\sin \alpha_3 = \sin(\theta'_2 - \theta_3 + \pi) \simeq 0$, we have from Eqs. (B15) and (B18) that

$$s_3 \xi_{3\varphi} = -b_2 s_2 \xi_{2\varphi} \simeq \frac{b_2 \xi_{1\varphi}}{\tan \theta_1 \cos \theta_2}. \quad (\text{B19})$$

Similarly, taking $S_{4,3} = +1$, $\cos \theta'_3 \ll 1$, and $\sin \alpha_4 = \sin(\theta'_3 + \theta_4) \simeq \sin(\pi/2 + \theta_4) \simeq \cos \theta_4$, we obtain from Eqs. (B15) and (B19):

$$\begin{aligned} s_4 \xi_{4\varphi} &= b_3 s_3 \xi_{3\varphi} + \frac{\phi_{3\varphi}^2}{2} \frac{\cos \theta'_3}{\cos \theta_4} \sin \alpha_4 \\ &\simeq -\frac{(1 - b_3 b_2) \xi_{1\varphi}}{\tan \theta_1 \cos \theta_2}. \end{aligned} \quad (\text{B20})$$

Finally, from Eqs. (B20) and (B5), we have for the angular spread $\xi'_{4\varphi} = \theta'_{4\varphi} - \theta'_4$ after the 4th crystal

$$\xi'_{4\varphi} = s_4 b_4 \xi_{4\varphi} = \Xi_4 \xi_{1\varphi}, \quad (\text{B21})$$

where

$$\Xi_4 \simeq -\frac{b_4(1 - b_3 b_2)}{\tan \theta_1 \cos \theta_2}. \quad (\text{B22})$$

Appendix C: Abbe sine condition for Wolter-type parabola-parabola optic

Howells proposed using a Wolter-type double-reflection system for designing plane grating spectrometers with a good coma-free off-axis imaging satisfying the Abbe sine condition [47]. Unlike the original proposal of Wolter, Howells suggested a double-mirror parabola-parabola configuration. Such a mirror combination has the great advantage of producing parallel x-rays between the two reflections at the parabolas, see Fig. 13, which is perfect for the proper performance of a plane diffraction grating inserted between the collimating and focusing mirrors in the spectrometer. The parallel rays between the collimating and focusing mirrors in the parabola-parabola configuration is also perfect for the CDDW-type flat-crystal dispersing elements considered in the present paper for the x-ray echo spectrometers.

Here we show that the Abbe sine condition

$$\sin \alpha / \sin \alpha' = \text{const} \quad (\text{C1})$$

is satisfied exactly for all rays only for a system with two identical parabolas producing one-to-one imaging. Here

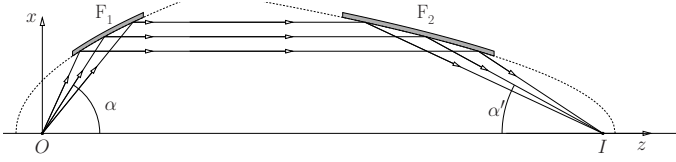


FIG. 13: Wolter-type double-reflection imaging optic comprising two parabolic mirrors F_1 and F_2 .

α and α' are angles of the rays to the optical axis emanating from the object point O and converging to the image point I , respectively, see Fig. 13. In a more general case of a system with two arbitrary parabolas, the sine condition may be satisfied to a very good accuracy, in particular, in cases of interest for x-ray echo spectrometer applications.

We consider x-rays reflected from the first parabolic mirror with the surface given by $x^2 = 2pz + p^2$, where p is a parabola parameter. X-rays reflected at a glancing angle of incidence γ make an angle $\alpha = 2\gamma$ with the optical axis, see Fig. 13, whose sine is

$$\sin \alpha = \frac{2px}{x^2 + p^2}. \quad (C2)$$

The same ray being reflected from the second mirror with parabolic surface given by $x^2 = 2p'x + (p')^2$ makes an

angle α' with the optical axis. The ratio of the sines is

$$\frac{\sin \alpha}{\sin \alpha'} = \frac{p}{p'} \frac{1 + (p'/x)^2}{1 + (p/x)^2}. \quad (C3)$$

If the parabolas are identical, i.e., $p = p'$, then $\sin \alpha / \sin \alpha' = 1$ and the Abbe sine condition is perfectly fulfilled for all rays, i.e., the system is “aplanatic”, capable of imaging without coma aberrations.

If the parabolas are not identical, i.e., $p \neq p'$, but $p/x \ll 1$ and $p'/x \ll 1$, then Eq. (C4) can be approximated by

$$\frac{\sin \alpha}{\sin \alpha'} \simeq \frac{p}{p'} \left[1 + \frac{(p')^2 - p^2}{x^2} \right]. \quad (C4)$$

For the mirrors with $\gamma = \alpha/2 \simeq 30$ mrad and the focal lengths, considered in Sec. X A, the typical ratios are $(p/x)^2 \lesssim 10^{-3}$ at the mirrors' centers, and the variations are $(p/x)^2 \lesssim 10^{-4}$ over the whole range of x along the mirrors.

Therefore, in the particular cases of interest for x-ray echo spectrometers, the Abbe sine condition for the Wolter-type parabola-parabola system can be fulfilled with a very good accuracy even if two different parabolic mirrors are used.

-
- [1] Yu. Shvyd'ko, Phys. Rev. Lett. **116**, 080801 (2016).
 - [2] E. Burkel, B. Dorner, and J. Peisl, Europhys. Lett. **3**, 957 (1987).
 - [3] E. Burkel, *Inelastic Scattering of X rays with Very High Energy Resolution*, vol. 125 of *Springer Tracts in Modern Physics* (Springer, Berlin, 1991).
 - [4] F. Sette, M. H. Krisch, C. Masciovecchio, G. Ruocco, and G. Monaco, Science **280**, 1550 (1998).
 - [5] E. Burkel, Rep. Prog. Phys. **63**, 171 (2000).
 - [6] M. Krisch and F. Sette, *Light Scattering in Solids IX* (Springer, Berlin, 2007), vol. 108 of *Topics in Applied Physics*, chap. Inelastic X-Ray Scattering from Phonons, pp. 317–370.
 - [7] G. Monaco, *Synchrotron Radiation* (Springer Berlin Heidelberg, 2015), chap. The High-Frequency Atomic Dynamics of Disordered Systems Studied by High-Resolution Inelastic X-Ray Scattering, pp. 461–482.
 - [8] A. Q. R. Baron, *Synchrotron Light Sources and Free-Electron Lasers* (Springer International Publishing, 2016), chap. 52-1 Introduction to High-Resolution Inelastic X-Ray Scattering, pp. 1–32, arXiv:1504.01098.
 - [9] O. Chubar, G. Geloni, V. Kocharyan, A. Madsen, E. Saldin, S. Serkez, Yu. Shvyd'ko, and J. Sutter, Journal of Synchrotron Radiation **23**, 410 (2016).
 - [10] T. S. Toellner, A. Alatas, and A. H. Said, Journal of Synchrotron Radiation **18**, 605 (2011).
 - [11] A. H. Said, H. Sinn, and R. Divan, Journal of Synchrotron Radiation **18**, 492 (2011).
 - [12] H. Kogelnik and T. Li, Appl. Opt. **5**, 1550 (1966).
 - [13] T. Matsushita and U. Kaminaga, Journal of Applied Crystallography **13**, 472 (1980).
 - [14] A. E. Siegman, *Lasers* (University Science Books, Sausalito, California, 1986).
 - [15] E. L. Hahn, Phys. Rev. **80**, 580 (1950).
 - [16] F. Mezei, ed., *Neutron Spin Echo.*, vol. 128 of *Lecture Notes in Physics* (Springer, Berlin, 1980).
 - [17] Yu. Shvyd'ko and R. Lindberg, Phys. Rev. ST Accel. Beams **15**, 100702 (2012).
 - [18] H. S. Fung, C. T. Chen, L. J. Huang, C. H. Chang, S. C. Chung, D. J. Wang, T. C. Tseng, and K. L. Tsang, AIP Conf. Proc. **705**, 655 (2004).
 - [19] C. H. Lai, H. S. Fung, W. B. Wu, H. Y. Huang, H. W. Fu, S. W. Lin, S. W. Huang, C. C. Chiu, D. J. Wang, L. J. Huang, et al., Journal of Synchrotron Radiation **21**, 325 (2014).
 - [20] W. Schülke, H. Nagasawa, S. Mourikis, and P. Lanzki, Phys. Rev. B **33**, 6744 (1986).
 - [21] W. Schülke, Nucl. Instrum. Methods Phys. Res. A **246**, 491 (1986).
 - [22] W. Schülke, *Electron dynamics by inelastic X-ray scattering* (Oxford University Press, 2007).
 - [23] P. Suortti, T. Buslaps, M. DiMichiel, V. Honkimäki, U. Lienert, J. McCarthy, J. Merino, and A. Shukla, Nucl. Instrum. Methods Phys. Res. A **467-468**, 1541 (2001).
 - [24] Yu. Shvyd'ko, *X-Ray Optics – High-Energy-Resolution Applications*, vol. 98 of *Optical Sciences* (Springer, Berlin, 2004).
 - [25] Yu. V. Shvyd'ko, M. Lerche, U. Kuetgens, H. D. Rüter,

- A. Alatas, and J. Zhao, Phys. Rev. Lett. **97**, 235502 (2006).
- [26] Yu. Shvyd'ko, S. Stoupin, D. Shu, S. P. Collins, K. Mundboth, J. Sutter, and M. Tolkiehn, Nature Communications **5** (2014).
- [27] Yu. Shvyd'ko, Phys. Rev. A **91**, 053817 (2015).
- [28] T. Matsushita and U. Kaminaga, Journal of Applied Crystallography **13**, 465 (1980).
- [29] Yu. Shvyd'ko, S. Stoupin, K. Mundboth, and J. Kim, Phys. Rev. A **87**, 043835 (2013).
- [30] Yu. Shvyd'ko, S. Stoupin, D. Shu, and R. Khachatryan, Phys. Rev. A **84**, 053823 (2011).
- [31] S. Stoupin, Yu. V. Shvyd'ko, D. Shu, V. D. Blank, S. A. Terentyev, S. N. Polyakov, M. S. Kuznetsov, I. Lemesch, K. Mundboth, S. P. Collins, et al., Opt. Express **21**, 30932 (2013).
- [32] A. Suvorov and Y. Q. Cai, Proc. SPIE **9963**, 99630A (2016).
- [33] B. Lengeler, C. Schroer, J. Tümmeler, B. Benner, M. Richwin, A. Snigirev, I. Snigireva, and M. Drakopoulos, J. Synchrotron Radiation **6**, 1153 (1999).
- [34] H. Yumoto, T. Koyama, S. Matsuyama, Y. Kohmura, K. Yamauchi, T. Ishikawa, and H. Ohashi, Synchrotron Radiation News **29**, 27 (2016).
- [35] P. Kirkpatrick and A. V. Baez, J. Opt. Soc. Am. **38**, 766 (1948).
- [36] M. Montel, *X-ray Microscopy and Microradiography* (Academic Press, New York, 1957), chap. X-ray Microscopy with Catamegonic Roof Mirrors, pp. 177–185.
- [37] Y. Platonov (2017), RIGAKU USA, *private communication*.
- [38] K. Mundboth, J. Sutter, D. Laundry, S. Collins, S. Stoupin, and Yu. Shvyd'ko, J. Synchrotron Radiation **21**, 16 (2014).
- [39] M. Born and E. Wolf, *Principles of Optics* (Cambridge University Press, Cambridge, 1999).
- [40] B. Aschenbach, Exp. Astron. **26**, 95 (2009).
- [41] J. E. Harvey, *Atmospheric Optics, Modulators, Fiber Optics, X-Ray and Neutron Optics* (McGraw Hill Professional, 2010), vol. V of *Handbook of Optics*, chap. Image Formation with Grazing Incidence Optics, p. 44.3, 3rd ed.
- [42] H. Wolter, Annalen der Physik **445**, 94 (1952).
- [43] H. Wolter, Annalen der Physik **445**, 286 (1952).
- [44] R. Kodama, Y. Katori, T. Iwai, N. Ikeda, Y. Kato, and K. Takeshi, Opt. Lett. **21**, 1321 (1996).
- [45] S. Matsuyama, Y. Emi, H. Kino, Y. Kohmura, M. Yabashi, T. Ishikawa, and K. Yamauchi, Opt. Express **23**, 9746 (2015).
- [46] J. Yamada, S. Matsuyama, Y. Sano, and K. Yamauchi, Appl. Opt. **56**, 967 (2017).
- [47] M. R. Howells, Nuclear Instruments and Methods **177**, 127 (1980).
- [48] A. Schubert, A. Bergamaschi, C. David, R. Dinapoli, S. Elbracht-Leong, S. Gorelick, H. Graafsma, B. Henrich, I. Johnson, M. Lohmann, et al., Journal of Synchrotron Radiation **19**, 359 (2012).
- [49] R. Dinapoli, A. Bergamaschi, S. Cartier, D. Greiffenberg, I. Johnson, J. H. Jungmann, D. Mezza, A. Mozzanica, B. Schmitt, X. Shi, et al., Journal of Instrumentation **9**, C05015 (2014).
- [50] M. Borland, *Preliminary Expected Performance Characteristics of an APS Multi-Bend Achromat Lattice*, Advanced Photon Source, ANL/APS/LS-337, CVS revision 1.30 ed. (2014), <https://www1.aps.anl.gov/files/download/Aps-Upgrade/multi-bend-achromat-lattice.pdf>.